ELSEVIER

J. Non-Newtonian Fluid Mech. 133 (2006) 35–56

Journal of Non-Newtonian Fluid Mechanics

www.elsevier.com/locate/jnnfm

Transient squeeze flow of viscoplastic materials

George Karapetsas, John Tsamopoulos *

Laboratory of Computational Fluid Dynamics, Department of Chemical Engineering, University of Patras, Patras 26500, Greece

Received 14 June 2005; received in revised form 28 September 2005; accepted 1 October 2005

Abstract

The transient, axisymmetric squeezing of viscoplastic materials under creeping flow conditions is examined. The flow of the material even outside the disks is followed. Both cases of the disks moving with constant velocity or under constant force are studied. This time-dependent simulation of squeeze flow is performed for such materials in order to determine very accurately the evolution of the force or the velocity, respectively, and the distinct differences between these two experiments, the highly deforming shape and position of all the interfaces, the effect of possible slip on the disk surface, especially when the slip coefficient is not constant, and the effect of gravity. All these are impossible under the quasi-steady state condition used up to now. The exponential constitutive model, suggested by Papanastasiou, is employed. The governing equations are solved numerically by coupling the mixed finite element method with a quasi-elliptic mesh generation scheme in order to follow the large deformations of the free surface of the fluid. As the Bingham number increases, large departures from the corresponding Newtonian solution are found. When the disks are moving with constant velocity, unyielded material arises only around the two centers of the disks verifying previous works in which quasi-steady state conditions were assumed. The size of the unyielded region increases with the Bingham number, but decreases as time passes and the two disks approach each other. Their size also decreases as the slip velocity or the slip length along the disk wall increase. The force that must be applied on the disks in order to maintain their constant velocity increases significantly with the Bingham number and time and provides a first method to calculate the yield stress. On the other hand, when a constant force is applied on the disks, they slow down until they finally stop, because all the material between them becomes unyielded. The final location of the disk and the time when it stops provide another, probably easier, method to deduce the yield stress of the fluid.

Keywords: Transient squeeze flow; Viscoplastic fluids; Free surface flows

1. Introduction

Squeeze flow is widely used as a typical experiment for the rheological characterization of non-Newtonian fluids [1]. It is also encountered in various engineering processes like compression molding, which is used for the manufacturing of various industrial parts [2]. The rheological experiment can be performed in two different ways, either by measuring the force required to push the disks at a constant velocity [3–5] or by measuring the velocity of the disks towards each other when a constant force is applied [6–8]. Our efforts here are aimed at developing an accurate and efficient numerical method in order to simulate both versions of such a rheological experiment for the special case of a viscoplastic material.

The deformation and flow of viscoplastic materials are very important, since many multicomponent fluids such as suspensions, pastes, paints, foodstuffs, foams and slurries, which are very frequently encountered in industrial processes, are viscoplastic [9]. These materials exhibit small or no deformation at all (solid-like behavior) when the applied stress is below a particular value, which is called yield stress. Above the yield stress, they flow with viscosity that depends on the local rate of strain. Whether yield stress really exists is a subject that has drawn some attention [10], however it is widely accepted that this concept, when it is used properly, can provide an accurate description of physical phenomena and industrial processes.

The first constitutive law that was proposed for describing the flow of such materials is the Bingham model [11]. Its application is extended to more than one dimensions through the Von Mises criterion for dividing the domain occupied by the material in regions where it behaves either as rigid solid or as liquid. When two such regions coexist in a domain this criterion introduces a discontinuity in the constitutive law at the yield surface, which

* Corresponding author. Fax: +30 2610 996 178.
E-mail address: tsamo@chemeng.upatras.gr (J. Tsamopoulos).

0377-0257/$ – see front matter © 2005 Elsevier B.V. All rights reserved.
doi:10.1016/j.jnnfm.2005.10.010

is the location where these two regions meet. Moreover, when the flow is multi-dimensional or time-dependent, this discontinuity usually leads to considerable computational problems, because in such cases it is very difficult to predict correctly the location and the shape of the yield surface. It is characteristic that although this model is used extensively for simple and steady flows, very few researchers have used it in more complex flows. Such an exception is the work by Beris et al. [12], who presented a numerical simulation for the creeping flow around a moving sphere. Although at first sight this problem does not seem to be so complicated, it required a very careful analysis in order to reveal that unyielded material arises around the two stagnation points of flow and at some finite distance from the sphere. Alternatively, Frigaard and co-workers have advanced the augmented Lagrangian method as a viable alternative to deal with such problems [13]. To avoid difficulties like these, various modifications of the Bingham constitutive equation have been introduced. Two such modifications are the biviscosity model, proposed by O'Donovan and Tanner [14] and the exponential model, proposed by Papanastasiou [15]. In the present analysis we decided to use the Papanastasiou model which has the following form:

$$\underline{\underline{\tau}}^* = -\left[\eta_0 + \frac{\tau_y(1-\mathrm{e}^{-m\dot{\gamma}^*})}{\dot{\gamma}^*}\right]\underline{\underline{\dot{\gamma}}}^* \tag{1}$$

where the superscript (*) denotes a dimensional quantity, $\underline{\underline{\tau}}^*$ is the extra stress tensor, η_0 is the plastic viscosity, $\underline{\underline{\dot{\gamma}}}^*$ is the rate of strain tensor defined as $\underline{\underline{\dot{\gamma}}}^* = \nabla\underline{v}^* + (\nabla\underline{v}^*)^{\mathrm{T}}$, $\dot{\gamma}^*$ is its second invariant, $\dot{\gamma}^* = [(1/2)\underline{\underline{\dot{\gamma}}}^* : \underline{\underline{\dot{\gamma}}}^*]^{1/2}$, and m is the stress growth exponent.

Smyrnaios and Tsamopoulos [16] have shown that for relatively large values (depending on the flow at hand) of the exponent coefficient, m, this model closely approximates the discontinuous Bingham behavior. On the other hand, Burgos et al. [17] have suggested that extremely large values of this coefficient should be avoided for reasons that have to do with numerical stability and the stiffness of the resulting discrete system. The main advantage of this constitutive equation is the fact that it is continuous and it holds uniformly in yielded and unyielded regions. Thus the determination of the shape and the location of the yield surface can be performed a posteriori instead of simultaneously with the flow, as required by the discontinuous Bingham model [12]. We explain the method we have followed for its determination in Section 3.4. Moreover, this model has a continuous dependence of the stress on $\underline{\underline{\dot{\gamma}}}^*$, which has been argued to be more meaningful physically [18]. On the other hand, the yield surface, for example, is expected not to coincide completely with that determined following the discontinuous Bingham model.

Many researchers have employed the aforementioned models in order to simulate the viscoplastic behavior in complex or even in time-dependent flows, but we will mention here only some characteristic examples. Jay et al. [19] have used the biviscosity model to study the flow through a sudden axisymmetric expansion and provided some very interesting comparisons with experimental observations. The Papanastasiou model has been used in transient simulations by Tsamopoulos et al. [20] to study the thinning of a viscoplastic fluid film on a rotating disk in the process of spin coating and by Dimakopoulos and Tsamopoulos [21] to study the displacement of a viscoplastic material by air in straight and suddenly constricted tubes.

The behavior of viscoplastic materials in squeeze flow has attracted the attention of several researchers in the past. In early theoretical studies, the most usual approach was the lubrication approximation. This approach is still used today to evaluate experimental results, although it was noticed almost from the beginning that it led to profound kinematic inconsistencies in the calculated velocity fields [16,22]. O'Donovan and Tanner [14] were the first who recognized the need to solve the squeeze film problem without using the lubrication approximation. They solved numerically the constant velocity problem employing the biviscosity model for describing the viscoplastic behavior of the material and they finally concluded that unyielded material arises only adjacent to the center of the plates. Quite recently Smyrnaios and Tsamopoulos [16] provided a qualitative analysis and accurate numerical simulations for this problem assuming quasi-steady state conditions. They employed both the original Bingham constitutive equation and the exponential one to definitively clarify all the misleading speculations about the position and the existence of yield surfaces in this flow field. They showed that unyielded material could only exist around the two stagnation points of flow extending in this way the work by O'Donovan and Tanner [14]. Matsoukas and Mitsoulis [23] also solved numerically the squeeze flow of viscoplastic materials, assuming quasi-steady state, for both planar and axisymmetric flow, confirming the earlier results by Smyrnaios and Tsamopoulos [16]. They have also provided a more accurate correlation for the force that must be applied on the disks' surface in order to maintain their constant velocity. The only transient simulations of non-Newtonian fluids undergoing squeeze flow that we are aware of are those by Mavridis et al. [24], albeit for a power-law fluid.

In the present work, we solve the transient squeeze flow of a viscoplastic material for both cases where the disks are moving with constant velocity and under constant force. Clearly, this distinction is impossible under the quasi-steady state conditions. The transient simulation enables the determination of the transient force or velocity, respectively, the shape of the liquid/air interface, and the location of the yield surface, at every time instant. Moreover we are able to study the effect on the process of possible slip of the fluid on the disk surface and also the effect of gravity.

The remainder of the paper is organized as follows. In Section 2, we present the governing equations and the boundary conditions for this problem. The numerical algorithm, used in our simulations, is described in Section 3. In Section 4, we present the results of the extensive parametric analysis that we performed for a viscoplastic fluid that is being squeezed either with constant disk velocity or under constant force. Finally, conclusions of the present study are drawn in Section 5.

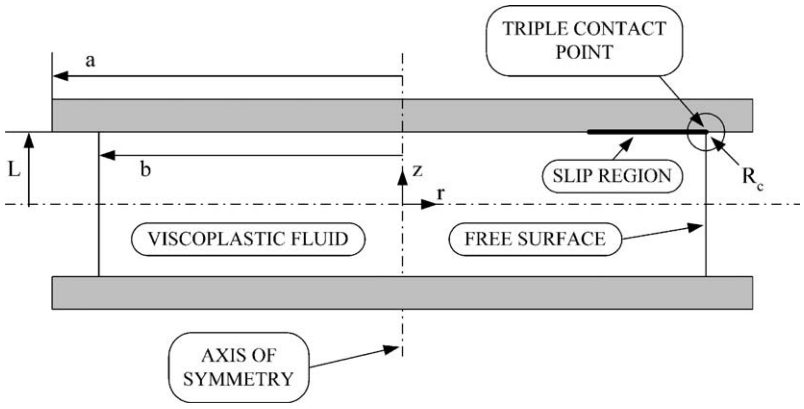

Fig. 1. Schematic of the squeeze flow geometry between two parallel coaxial disks.

2. Problem formulation

We consider the axisymmetric squeeze flow of a viscoplastic material with a constant yield stress, τ_y, and upon yielding a constant dynamic viscosity, η_0. We assume that the fluid is incompressible with constant density, ρ and its interface with the surrounding air has an interfacial tension, σ. Fig. 1 illustrates a schematic of the flow geometry examined herein: the space between two parallel, coaxial disks with radius a is filled with a viscoplastic material, which forms another cylinder coaxial to the two disks. The radius of this sample is denoted with b and, generally, $b \leq a$. Initially the disks are stationary and the free surface of the fluid is assumed to be a perfect cylindrical one. Consequently, the pressure inside the fluid is uniform initially, while the ambient pressure is taken to be zero.

Squeeze flow experiments are usually conducted in two different ways: the disks are moving either with constant velocity or under constant force. Both versions are examined in this work. At startup of the constant velocity experiment, the velocity of the disks is increased abruptly from zero to V, whereas at start up of the constant force problem, the constant force F is applied on the surface of the disks. In both cases therefore, the disk displacement sets the fluid in motion and deforms the domain of the material. We scale all lengths with half the initial distance of the two disks, L, and time with L/V^*, where V^* is the characteristic velocity. For the constant velocity case the choice of the characteristic velocity V^* is obvious and it is the constant velocity of the disks V. On the other hand, although no characteristic velocity exists for the constant force case, due to the decelerating nature of the flow, we have chosen as such the initial velocity of the disks $V(t=0^+)$. In addition, both pressure and stress components are scaled with a viscous scale $\eta_0 V^*/L$, whereas the force applied on the disk is scaled with $\eta_0 V^* L\pi/\varepsilon^2$. Thus, the dimensionless groups that arise are the Reynolds number, the Bingham number, the capillary number, the Stokes number, when gravity is taken under consideration, and, finally, the aspect ratios of the volume initially occupied by the material or of the total volume between the disks, respectively. The definitions of these numbers and their typical values are given in Table 1.

The flow of an incompressible fluid is governed by the momentum and mass conservation equations, which in their dimensionless form are:

$$Re\frac{\mathrm{D}\underline{v}}{\mathrm{D}t} + \underline{\nabla}P + \underline{\nabla}\cdot\underline{\underline{\tau}} + St\,\underline{e}_z = 0 \tag{2}$$

$$\underline{\nabla}\cdot\underline{v} = 0 \tag{3}$$

where $\underline{\underline{\tau}}$ is the viscous part of the total stress tensor $\underline{\underline{\sigma}}$,

$$\underline{\underline{\sigma}} = P\underline{\underline{I}} + \underline{\underline{\tau}}, \tag{4}$$

$\underline{v}$, P are the axisymmetric velocity vector and the pressure, respectively, while D/Dt denotes the material derivative and ∇ the gradient operator. Under typical experimental conditions for viscoplastic materials, creeping flow conditions prevail and hereafter we will take $Re = 0$. To complete the description of the flow problem a constitutive equation that describes the rheology of the fluid is required. In the present study we employ the continuous constitutive equation that has been proposed by Papanastasiou [15] which relates the stress tensor, $\underline{\underline{\tau}}$, to the rate of strain tensor, $\underline{\underline{\dot{\gamma}}}$, by a simple exponential relation. The dimensionless form of this constitutive equation is

$$\underline{\underline{\tau}} = -\left[1 + Bn\frac{1-\mathrm{e}^{-N\dot{\gamma}}}{\dot{\gamma}}\right]\underline{\underline{\dot{\gamma}}} \tag{5}$$

where $\underline{\underline{\dot{\gamma}}}$ is the rate of strain tensor defined as $\underline{\underline{\dot{\gamma}}} = \underline{\nabla v} + \underline{\nabla v}^{\mathrm{T}}$, $\dot{\gamma}$ is its second invariant, $\dot{\gamma} = [(1/2)\underline{\underline{\dot{\gamma}}} : \underline{\underline{\dot{\gamma}}}]^{1/2}$ and N is the stress

Table 1
Definitions of dimensionless numbers arising in the present model and their typical values

Dimensionless number	Definition	Realistic values
Reynolds	$Re = \dfrac{\rho V L}{\eta_0}$	$Re \ll 1$
Bingham	$Bn = \dfrac{\tau_y L}{\eta_0 V}$	$0 < Bn < 100$
Capillary	$Ca = \dfrac{\eta_0 V}{\sigma}$	$Ca \gg 1$
Stokes	$St = \dfrac{\rho g L^2}{\eta_0 V}$	$St < 1$
Initial disk aspect ratio	$\varepsilon = \dfrac{L}{b}$	$0 < \varepsilon \ll 1$
Initial material aspect ratio	$w = \dfrac{a}{L}$	$\varepsilon^{-1} \geq w \gg 1$

Table 2
Bingham numbers and corresponding dimensionless values for the exponential factor in the Papanastasiou model

Bn	1	10	30	50	100
N	500	500	300	300	300

growth exponent, $N = mV^*/L$. In the simulations to be presented in this paper, after careful evaluation, for the reasons explained earlier, we have chosen the values of N depending on the values of the Bingham number as shown in Table 2.

2.1. Boundary conditions

Along the free surface the velocity field should satisfy a local force balance between surface tension and viscous stresses in the liquid, setting the pressure in the surrounding gas to zero (datum pressure)

$$\underline{n} \cdot \underline{\underline{\sigma}} = \frac{2H}{Ca}\underline{n} \tag{6}$$

where $\underline{n}$ is the outward unit normal to the free surface and $2H$ is its mean curvature which is defined as

$$2H = -\underline{\nabla}_s \cdot \underline{n}, \quad \underline{\nabla}_s = (\underline{\underline{I}} - \underline{nn}) \cdot \underline{\nabla} \tag{7}$$

Taking the tangential and normal to the free surface components of this force balance we obtain

$$\underline{tn} : \underline{\underline{\sigma}} = 0 \tag{8}$$

$$\underline{nn} : \underline{\underline{\sigma}} = \frac{2H}{Ca} \tag{9}$$

In addition, the boundary conditions that must be imposed at the axis of symmetry ($r = 0$) are

$$\underline{n} \cdot \underline{v} = 0 \tag{10}$$

$$\underline{tn} : \underline{\underline{\sigma}} = 0 \tag{11}$$

When gravity is taken into consideration no other symmetry arises and the studied domain is the right half of the domain shown in Fig. 1. However, we have also performed simulations assuming that gravity is negligible and in that case a plane of symmetry arises as well. The studied domain now becomes the upper-right quarter of the space occupied by the material and the following conditions are imposed on the plane of symmetry ($z = 0$)

$$\underline{n} \cdot \underline{v} = 0 \tag{12}$$

$$\underline{tn} : \underline{\underline{\sigma}} = 0 \tag{13}$$

On the surface of the disk, two boundary conditions are imposed. In the axial direction, the boundary condition actually depends on the problem that is examined each time. In particular, for the constant velocity problem the fluid has the same axial velocity with the disks, and thus

$$\underline{n} \cdot \underline{v} = -1 \tag{14}$$

while for the constant force problem the conditions that must be imposed are

$$F - \int_0^{R_c} 2\pi\sigma_{zz} r \, dr = 0 \tag{15a}$$

where R_c is the radial distance of the triple contact point from the axis of symmetry, see Fig. 1. In addition, the fluid in contact with the disk must move with the same (instantaneous) disk velocity, which changes with time according to (15a):

$$\underline{n} \cdot \underline{v} = \text{const.} \tag{15b}$$

The vectors $\underline{n}$ and $\underline{t}$ in Eqs. (8)–(15) are defined with respect to the surface on which they apply. In the radial direction either the usual no-slip condition, $v_r = 0$, or a suitable slip model is applied. Slip is very often encountered in processing of non-Newtonian materials. Especially in the flow of solid suspensions, which in many cases exhibit viscoplastic behavior, an additional reason for apparent slip is the displacement of the dispersed phase away from the solid boundaries, leaving a layer of liquid with lower effective viscosity near them. Thus, the separated liquid near the wall acts like a lubricant for the rest of the material and this is often interpreted as slip [25]. Another reason for introducing slip arises from the fact that when the triple contact points (or rather contact lines, at the intersection of the material/air interface with the disks) are moving and a no-slip condition is applied along the solid walls, the velocity there is not single-valued, which gives rise to a non-physical stress singularity. Although the resolution of this problem is still under investigation, the most common approach is the assumption of local slip between the liquid and the solid surface near the contact point, in order to eliminate the stress singularity.

A number of slip conditions with variable degrees of complexity have been employed in the past for modeling flows of non-Newtonian materials [26,27]. In the present study, we adopt a modification of the slip model that was originally proposed by Kamal et al. [28]. This model divides the wall boundary into a slip region and a no-slip region. To this end, the slip coefficient is an exponential function of the radial distance from the triple contact point and in this way it achieves a continuous transition between the slip and the no-slip region. Thus, the slip model has the following form:

$$\underline{tn} : \underline{\underline{\sigma}} = \beta_{sl} \, e^{-\alpha_{sl}(r - R_c)} \underline{t} \cdot \underline{v} \tag{16}$$

where β_{sl} is a parameter used to adjust the level of slip velocity in comparison to the wall shear and α_{sl} is a second parameter used to adjust the length of the slip region. Furthermore, this model reduces to the no-slip condition as these two parameters increase, whereas when α_{sl} becomes zero the model reduces to the standard Navier slip model [29] and slip occurs over the entire wall boundary with a constant slip coefficient.

The model is completed by assuming that the fluid initially is at rest $\underline{v}(r, z, t = 0) = 0$, the free surface is flat with dimensionless radius b/L and that the fluid is under constant pressure

$$P(r, z, t = 0) = \frac{\varepsilon}{Ca} \tag{17}$$

3. Numerical implementation

In order to solve numerically the above set of equations we have chosen the mixed finite element method combined with an elliptic grid generation scheme for the discretization of the transient physical domain.

3.1. Elliptic grid generation

We employ the quasi-elliptic mesh generation scheme that has been recently developed and applied in various problems by Dimakopoulos and Tsamopoulos [30–32]. Here we will only present our adaptation of its essential features to the current problem. The interested reader may refer to Dimakopoulos and Tsamopoulos [30] for further details on all the important issues of the method. With this scheme the time-dependent physical domain (r, z) is mapped onto a fixed with time computational one (η, ξ). A fixed computational mesh is generated in the latter while, through the mapping, the corresponding mesh in the physical domain follows its deformations. Since the mesh in the physical domain moves, but not necessarily with the local fluid velocity, this method belongs to the group of ALE (Arbitrary Langrangian–Eulerian) methods. As computational domain we choose here the volume that is initially occupied by the fluid. This mapping is based on the solution of the following system of quasi-elliptic partial differential equations:

$$\underline{\nabla} \cdot \left(\varepsilon_1 \sqrt{\frac{r_\xi^2 + z_\xi^2}{r_\eta^2 + z_\eta^2}} + (1 - \varepsilon_1) \right) \underline{\nabla} \xi = 0 \tag{18}$$

$$\underline{\nabla} \cdot \underline{\nabla} \eta = 0 \tag{19}$$

where the subscripts denote the differentiation with respect to the variable indicated and ε_1 is a parameter that controls the smoothness of the mapping relative to the degree of orthogonality demanded and it is adjusted by trial and error; here it is set to 0.1. In order to solve the above system of differential equations appropriate boundary conditions must be imposed. On the fixed boundaries, we impose the equations that define their position and the remaining degrees of freedom are used for equidistributing the nodes along the boundaries. In addition, along the moving interface we impose the kinematic equation

$$\frac{\mathrm{D}\underline{F}}{\mathrm{D}t} = \underline{v} \tag{20}$$

where $\underline{F} = r\underline{e}_r + z\underline{e}_z$ is the position vector of the free surface, together with a condition that requires the uniform distribution of the nodes along the free surface.

3.2. Mixed finite element method

The computational domain is discretized using triangular elements, by carefully splitting in two elements each rectangular element generated by the previous method, because triangles conform better to the large deformations of the transient physical domain and, when significantly distorted, they do not create the computational problems that the rectangular elements do. We approximate the velocity vector with quadratic Lagrangian basis functions, ϕ^i, and the pressure as well as the position vector with linear Lagrangian basis functions, ψ^i. We employ the finite element/Galerkin method, which results into the following weak forms of the momentum and mass balances

$$\int_\Omega \left[Re \frac{\mathrm{D}\underline{v}}{\mathrm{D}t} \phi^i + \nabla \phi^i \cdot \underline{\underline{\sigma}} + \phi^i \, St \, \underline{e}_z \right] \mathrm{d}\Omega + \int_\Gamma \left[\underline{n} \cdot \underline{\underline{\sigma}} \right] \phi^i \, \mathrm{d}\Gamma = 0 \tag{21}$$

$$\int_\Omega \psi^i \nabla \cdot \underline{v} \, \mathrm{d}\Omega = 0 \tag{22}$$

where $\mathrm{d}\Omega$ and $\mathrm{d}\Gamma$ are the differential volume and surface area, respectively. The surface integral that appears in the momentum equation is split into four parts, each one corresponding to a boundary of the physical domain and the relevant boundary condition is applied therein. In order to avoid dealing with the second order derivatives that arise in the boundary integral of the interface, through the definition of the mean curvature H, we use the following formulation, first proposed by Ruschak [33]:

$$2H\underline{n} = \frac{\mathrm{d}\underline{t}}{\mathrm{d}s} - \frac{\underline{n}}{R_2} \tag{23}$$

where the first term describes the change of the tangential vector along the free surface and R_2 is the second principal radius of the curvature, $R_2 = r\sqrt{r_\xi^2 + z_\xi^2}/z_\xi$.

We must also derive the weak form of the mesh generation equations. Thus after applying the divergence theorem we obtain.

$$\int_\Omega \left(\varepsilon_1 \sqrt{\frac{r_\xi^2 + z_\xi^2}{r_\eta^2 + z_\eta^2}} + (1 - \varepsilon_1) \right) \underline{\nabla} \xi \cdot \underline{\nabla} \psi^i \, \mathrm{d}\Omega = 0 \tag{24}$$

$$\int_\Omega \underline{\nabla} \eta \cdot \underline{\nabla} \psi^i \, \mathrm{d}\Omega = 0 \tag{25}$$

The resulting set of algebraic equations is solved with the following two-step Newton–Raphson/non-linear Gauss–Seidel iteration scheme. At each time step the momentum and mass balances are solved until convergence using the physical domain from the previous time step. Then, once the velocities and pressure are known, the new locations of the mesh points can be determined from the mesh generation equations and their boundary conditions. This procedure continues until convergence is achieved for both the flow and mesh equations. This is an effective method for decoupling the flow from the mesh generation problem because it results in considerably smaller Jacobian matrices, which are easier to handle. Finally, the set of algebraic equations is integrated in time with the Predictor-Corrector Euler method introducing an automatic adaptation of the time step for ensuring the convergence of the above iteration scheme and optimizing code performance. The iterations are terminated using a tolerance for the absolute error of the residual vector, which is set at 10^{-9}. The Jacobian matrix that results for the constant velocity case after each Newton iteration has a banded structure and the linearized

system is solved by Gaussian elimination using a banded matrix solver. However, the Jacobian matrix in the constant force case does not have a banded structure because Eq. (15) must be used which couples all the (unknown) velocities on the disk surface, instead of Eq. (14), which sets the velocity at each one of the nodes on the disk. This happens because the numbering of the nodes proceeds in the axial direction first, since the number of elements in that direction is much less than in the radial direction, and Eq. (15) gives to the Jacobian an "arrow" structure. In order to invert it efficiently and still take advantage of its large banded segment we split the Jacobian in four submatrices and the linear system becomes

$$\begin{bmatrix} \boldsymbol{A} & \boldsymbol{B} \\ \boldsymbol{C} & \boldsymbol{D} \end{bmatrix} \begin{bmatrix} \boldsymbol{x}_1 \\ \boldsymbol{x}_2 \end{bmatrix} = \begin{bmatrix} \boldsymbol{b}_1 \\ \boldsymbol{b}_2 \end{bmatrix} \tag{26}$$

where $\boldsymbol{b}_2$ is the single residual of Eq. (15), $\boldsymbol{C}$ and $\boldsymbol{D}$ its contributions to the Jacobian matrix and $\boldsymbol{b}_1$ is the residual vector of the rest of the equations and $\boldsymbol{A}$ and $\boldsymbol{B}$ its contributions to the same Jacobian matrix. This system is solved in a two-step process solving first for $\boldsymbol{x}_2$ and then for $\boldsymbol{x}_1$

$$\boldsymbol{S}\boldsymbol{x}_2 = \boldsymbol{b}_2 - \boldsymbol{C}\boldsymbol{A}^{-1}\boldsymbol{b}^{-1}, \quad \text{where } \boldsymbol{S} = \boldsymbol{D} - \boldsymbol{C}\boldsymbol{A}^{-1}\boldsymbol{B} \tag{27}$$

$$\boldsymbol{x}_1 = \boldsymbol{A}^{-1}\boldsymbol{b}_1 - \boldsymbol{A}^{-1}\boldsymbol{B}\boldsymbol{x}_2 \tag{28}$$

Once we compute the LU decomposition of matrix $\boldsymbol{A}$, which is a banded matrix, we need to compute the products $\boldsymbol{A}^{-1}\boldsymbol{B}$ and $\boldsymbol{A}^{-1}\boldsymbol{b}_1$ and this can be easily done by applying the back substitution step for multiple right-hand sides which are formed by the columns of the matrix $\boldsymbol{B}$ and the vector $\boldsymbol{b}_1$. The computation of the vector $\boldsymbol{C}\boldsymbol{A}^{-1}\boldsymbol{b}_1$ and of the matrix $\boldsymbol{S}$, when the matrix $\boldsymbol{C}$ is rather small, as it is in our case, is trivial. Having computed the vector $\boldsymbol{x}_2$ we can easily compute the remaining part of the unknowns, $\boldsymbol{x}_1$.

In order to compute accurately the large deformations of the physical domain we used 50 elements on the ξ-direction (axial) and 200 elements on the η-direction (radial), resulting in 20 000 triangular elements in the upper-right quarter of the domain and 50 752 unknowns including the two coordinates of the grid points. The initial time step in all the simulations is $\Delta t = 10^{-5}$. The code was written in Fortran 90 and was run on a workstation with dual Xeon CPU at 2.8 GHz in the Laboratory of Computational Fluid Dynamics. Each run typically required 2–3 days to complete.

3.3. Motion of the material/air interface towards the wall

While the disks move towards each other and as long as the free surface of the material moves inside the space between them, it is being deformed, and later on parts of it come very close to the solid wall and, eventually, into contact with it. Therefore, besides the usual motion of the contact point, a new contact point may be created ahead of the previous one. The calculation of this new contact point of the free surface with the disk wall, introduces an important technical difficulty to the simulation of the transient squeeze flow problem. This wetting process is simulated following the technique that was used by Poslinski and Tsamopoulos [34,35] to model the contact line motion in the blow molding process, i.e. the inflation of fluid annular menisci within a mold.

The basic idea of the method is to predict the time step Δt such that only the nearest to the wall node of the free surface, which at time t is at some small distance away from the wall, will just reach the solid boundary at time $t + \Delta t$. To this end, the following first-order approximation is used.

$$\Delta t = \min \left[(Z_\mathrm{w} - Z_\mathrm{f}) / \frac{\partial Z_\mathrm{f}}{\partial t} \right] \tag{29}$$

where Z_w denotes the position of the disk wall, Z_f is the axial position of the free surface node and $\partial Z_\mathrm{f}/\partial t$ is obtained by the following first-order formula:

$$\frac{\partial Z_\mathrm{f}}{\partial t} = \frac{Z_\mathrm{f} - Z_{\mathrm{f}0}}{t - t_0} \tag{30}$$

where $Z_{\mathrm{f}0}$ is the axial position of the free surface node at the previous time step. After a few iterations the distance between the disk wall and the free surface node becomes $|Z_\mathrm{w} - Z_\mathrm{f}| < 10^{-5}$. At the next time step, the force balance which was imposed on this node is replaced by the slip condition and the essential condition $v_z = -1$ in the case of the constant velocity problem or Eq. (15) in the case of a constant force simulation. As for the mesh generation, the kinematic equation is replaced by the essential condition $z = Z_\mathrm{w}$. If, in spite of these careful steps, the free surface node is displaced beyond the disk wall, the converged solution is rejected and the calculations are repeated with a smaller time step. Of course, as nodes from the free surface come into contact with the disk, their density on the free surface decreases, but not to the extend that the accuracy of the calculations is not acceptable. Clearly, this procedure is redundant when the material/air interface contacts the disks at their edge from the beginning, then the triple point is fixed at $R_\mathrm{c}^* = a$.

3.4. Yield surface determination

There are two different criteria that have been employed by several researchers in the past for determining the location of the yield surface. The first one determines this surface as the location where $\dot{\gamma}^* = 0$, while the second one as the location where $\tau^* = \tau_\mathrm{y}$. Quite recently Dimakopoulos and Tsamopoulos [21] argued that, following the Papanastasiou model, the two criteria are not equivalent and that it is more appropriate to use the second one, i.e. that the material flows when the second invariant of the extra stress tensor exceeds the yield stress. This criterion in its dimensionless form becomes

$$\text{yielded material}: \quad \tau > Bn \tag{31}$$

$$\text{unyielded material}: \quad \tau \leq Bn \tag{32}$$

Consequently, in order to determine the yield surface, the second invariant of the stress tensor must be calculated and this includes the computation of the velocity gradient tensor. As mentioned earlier however, the velocity field is discretized using Lagrangian basis functions, which means that the velocity gradient tensor is not continuous on the element sides and,

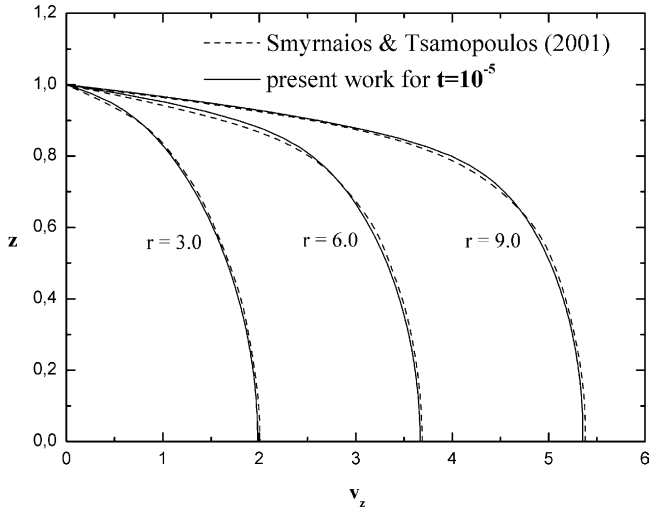

Fig. 2. Comparison of the predictions for the radial velocity profile at different radial positions for $Bn = 100$, $Re = 0$, $Ca = 10^3$, $w = 10$, $\varepsilon = 0.1$, $N = 300$ with results from the quasi-steady analysis and under the no-slip condition.

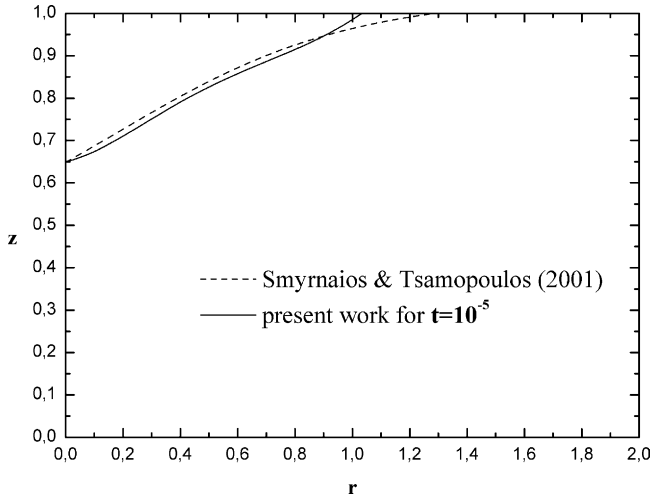

Fig. 3. Comparison of the predictions of the unyielded area with the present model for $Bn = 100$, $Re = 0$, $Ca = 10^3$, $w = 10$, $\varepsilon = 0.1$, $N = 300$ with results from the quasi-steady analysis and under the no-slip condition.

consequently, the direct computation at the nodes of the stress tensor is not possible. The most appropriate way to do this is to find a continuous approximation of the extra stress tensor by using the Galerkin projection method, that is

$$\int_{\Omega} \phi^i (\underline{\underline{T}} - \underline{\underline{\tau}}) \, \mathrm{d}\Omega = 0 \tag{33}$$

where $\underline{\underline{T}}$ denotes the continuous approximation of the stress tensor $\underline{\underline{\tau}}$. Now that the nodal values of the extra stress tensor are calculated the position of the yield surface can be easily determined. A similar procedure is followed to obtain contour lines of $\dot{\gamma}$ (e.g. on the yield surface, see Fig. 25).

4. Results and discussion

The squeeze flow of a liquid between two moving parallel coaxial disks depends on the dimensionless numbers that were mentioned earlier. More specifically, we examine the effects of the yield stress, the geometric aspect ratios, gravity and the magnitude of the slip coefficients on the disk walls. We start by validating our finite element code. Subsequently, in Section 4.2, we present simulations for the case that the disks are moving with constant velocity, while in Section 4.3 we present simulations for the case where the disks are moving under constant force.

4.1. Code validation

First, we verify the accuracy of our finite element code by comparing our results against the ones given by Smyrnaios and Tsamopoulos [16]. They used primarily the discontinuous Bingham model for solving the usual quasi-steady state model for the axisymmetric squeeze flow of a viscoplastic material with a constant disk velocity. In all quasi-steady models published so far, the presence and deformation of the free surface has been ignored. Fig. 2 compares their predictions with ours for the radial velocity profile at different radial positions, for $Bn = 100$, $Ca = 10^3$, $N = 300$ and when the no-slip condition is applied throughout the disk wall. The aspect ratios are $\varepsilon = 0.1$ and $w = 10$, which means that the initial radial distance of the free surface is 10 times the half distance between the two disks and the material initially occupies all the space between them. Of course, in the transient problem the distance between the two disks as well as the shape and radial distance of the free surface from the axis of symmetry change with time, in contrast to the quasi-steady state problem, where they are assumed to be constant. Because of this and in order to make the comparison possible and meaningful we have to make it at the very early stages of the transient simulation. To this end, we present a snapshot of the present simulations after the first time step, $t = 10^{-5}$. Clearly, the two studies provide virtually the same result for the radial velocity profiles.

To validate further our new code, we compared the location and the size of the unyielded area, for the same (initial) time instant and values of all the other parameters. Based on the discussion above, it is anticipated that the largest error will arise in calculating the yield surface. Fig. 3 focuses on only a part of the upper quarter of the domain between the disks in order to illustrate that the two results are very similar, in spite of the different formulations, mesh generation techniques and types of elements used in each one. The largest deviation in the yield surface location arises near the disk surface ($r \cong 1.1$) and there the current results are closer to those in Ref. [23], where the Papanastasiou model was used, as well. One could conclude that the quasi-steady state assumption, although it has certain shortcomings, like the inability to take into consideration the fluid/air interface and the actual deformation of the material, it provides a good understanding of the flow problem at least in its initial stage.

Finally, in Fig. 4, we present a blowup of the physical domain $[0 \le z \le z_d, 7.7 \le r]$ to illustrate the quality of the mesh produced following our method, even at so large deformations. For clarity reasons, we depict rectangular elements, although these have been divided in half to form triangular elements in order to bet-

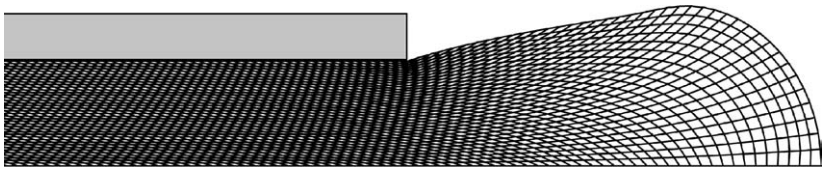

Fig. 4. The deformation of the mesh at $t = 0.4$ for $Bn = 1$, $Re = 0$, $Ca = 10^3$, $St = 0$, $w = 10$, $\varepsilon = 0.1$. For clarity we show rectangular elements for $r \geq 7.7$.

ter conform to large interface changes and avoid using highly deformed rectangular elements with all their negative consequences. Clearly, the mesh faithfully follows the interface and within the domain generates elements that vary in shape and size very smoothly. Moreover, they are more concentrated where they are needed the most: at edge of the disk.

4.2. Constant velocity case

4.2.1. Effect of the yield stress

To set the stage for the discussion that follows, it is useful to examine first the evolution of certain variables when a Newtonian fluid ($Bn = 0$) is undergoing squeeze flow. Fig. 5 illustrates the flow field in a fluid that initially fills completely the space between the disks, that is when $a = b = 10L$. Moreover capillarity is rather weak as is often the case in this process, $Ca = 10^3$, gravity is negligible, $St = 0$, and the no-slip condition is applied on the surface of the disks. The snapshots are taken at times $t = 0.2$, $t = 0.4$, $t = 0.7$ and each one of them shows the contour plots of the axial velocity, on the upper half, and the radial velocity, on the lower half. On the left hand side of each plot, we can see the axis of symmetry, while on the right-hand side we can see the interface between the fluid and air. We observe that the free surface, which initially was cylindrical, deforms everywhere even at early times.

The axial velocity has its smallest (negative) values at the upper disk because there the fluid follows the motion of the disks in the axial direction. However, its values monotonically increase towards zero at the mid-plane. In the three snapshots of this figure, the $[-1, 0]$ range of axial velocities between the disk and the mid-plane is divided in ten, eight and five equal intervals, respectively, by the lines of constant axial velocity. The total number of contour lines in this and all subsequent similar plots is 20. The axial velocity field changes drastically outside the disks. There, the squeezed out material is displaced slightly upwards near the upper disk due to the rearranging of the velocities and stresses, similarly to the extrudate swell phenomenon. This appears intensified by the downward motion of the corresponding disk. Therefore, the axial velocity has its largest and positive value near the edge of the upper disk and this value increases with time. At larger radial locations from where the axial velocity has its maximum (see Fig. 5), its values decrease towards zero, since no axial force is applied on the material there and viscous forces dissipate the flow.

As for the radial velocity component, it becomes zero on the axis of symmetry and on the surface of the disks because of the symmetry and the no-slip condition, respectively, while near the exit of the disks and at the mid-plane it has its largest values as the fluid is displaced primarily outwards in the radial direction. Its maximum value increases with time, as it should, because of

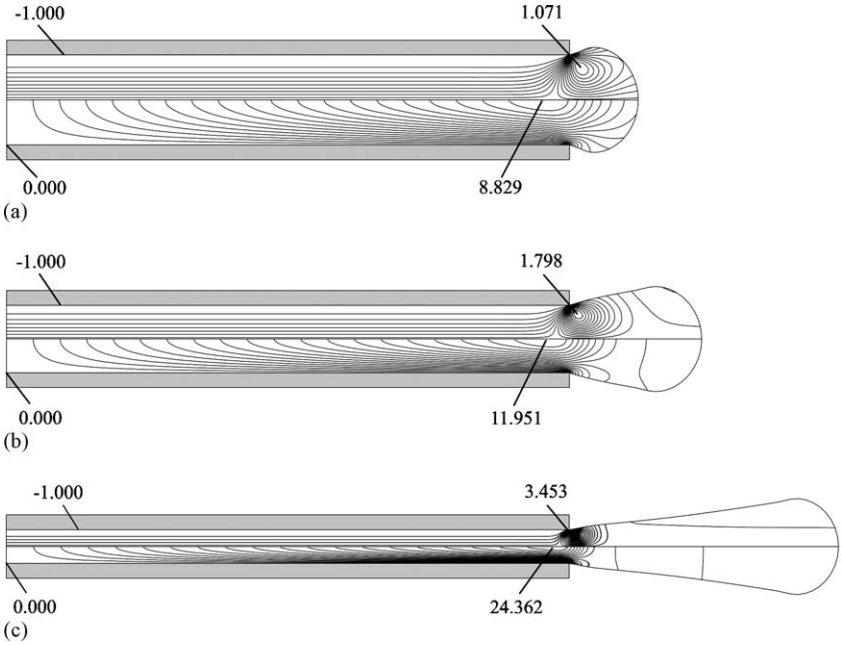

Fig. 5. Contour plots of the axial, upper half, and the radial, lower half, velocity component, at $t = 0.2$, $t = 0.4$, $t = 0.7$ for $Bn = 0$, $Re = 0$, $Ca = 10^3$, $St = 0$, $w = 10$, $\varepsilon = 0.1$ and under the no-slip condition.

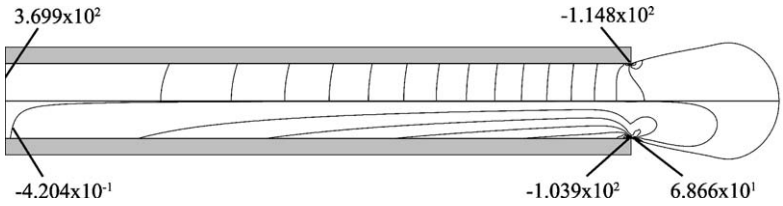

Fig. 6. Contour plots of the pressure, upper half, and τ_{rz}, lower half, at $t = 0.4$ for $Bn = 0$, $Re = 0$, $Ca = 10^3$, $St = 0$, $w = 10$, $\varepsilon = 0.1$ and under the no-slip condition.

the decreasing distance between the disks. The range of radial velocities from zero to its maximum value is divided in 20 equal intervals by the contour lines shown in each snapshot. Because of the radial and (smaller) axial expansion of the material outside the disks, mass conservation enforces a decrease of the radial velocity, which however, remains much larger than the axial component throughout the material. Away from the disk edge, the radial velocity drastically changes its spatial variation and decreases in the radial direction only. Even though interfacial tension is relatively small, it is still sufficient to make only the edge of the cross section of the free surface nearly semi-circular for this Newtonian fluid case, but leaves the material's upper and lower sides nearly straight and undeformed.

In spite of the initially small and decreasing aspect ratio, which should make the lubrication approximation even more accurate with time, it is evident from Fig. 5 that this approximation is never accurate enough near the disk edge and for a distance of the order of the disks' distance. The same is also evident in figures depicting the pressure or the stress distribution in the gap between the disks. Such plots demonstrate that the pressure is a function of the radial coordinate only, except near the edge of the disks. In Fig. 6 for example, we present the pressure (upper half) and shear stress (lower half) contour lines under the same conditions as in Fig. 5, but for $t = 0.4$ only, for conciseness. We can observe the 1D character of the pressure field almost up to the edge of the disk and the strong singularity in the shear stress at the edge of the disk where the transition from the no slip to the shear free condition takes place. Of course, this should have been expected because the basic assumption of the lubrication approximation, $b \gg L$, breaks down in that region, necessitating a two-dimensional analysis there.

It is anticipated that changing the rheological properties of the material should directly affect some of the characteristics of the flow. Fig. 7 illustrates the contour plots of the pressure on the upper half and the second invariant of the rate of strain tensor, $\dot{\gamma}$, on the lower half for a viscoplastic material with $Bn = 100$, at times $t = 0.2$, $t = 0.4$, $t = 0.6$. The same geometric, capillary and gravitational parameters are used as in the previous Newtonian case, while the dimensionless constant in the exponent of the Papanastasiou model is large enough based on our tests, $N = 300$, see Table 2. As one can see clearly, the shape of the free surface has changed. The viscoplastic property of the present material

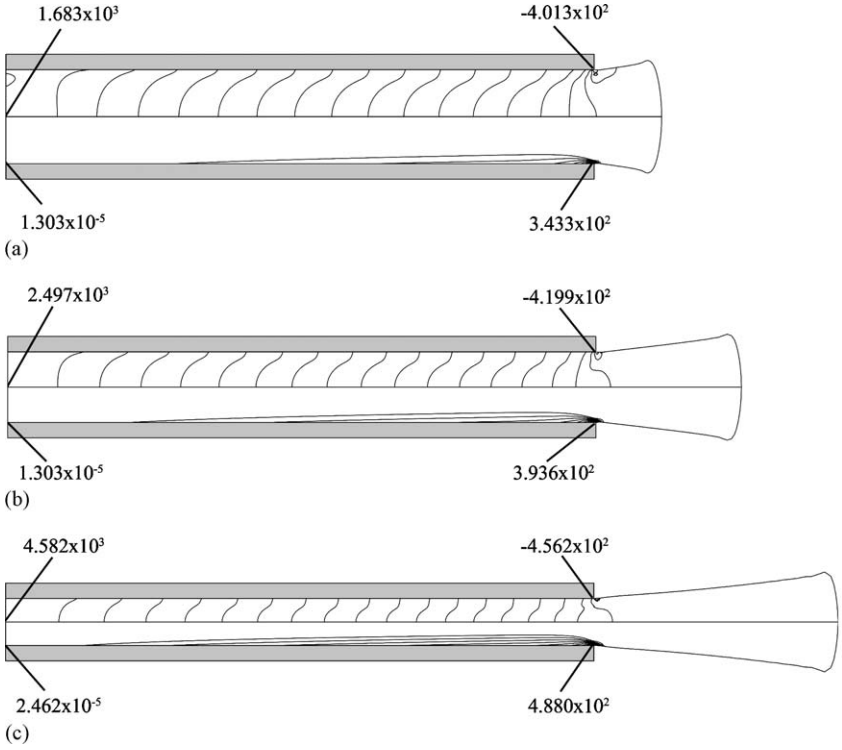

Fig. 7. Contour plots of the pressure field, upper half, and the second invariant of the rate of strain tensor, lower half, at $t = 0.2$, $t = 0.4$, $t = 0.6$ for $Bn = 100$, $Re = 0$, $Ca = 10^3$, $St = 0$, $w = 10$, $\varepsilon = 0.1$, $N = 300$ and under the no-slip condition.

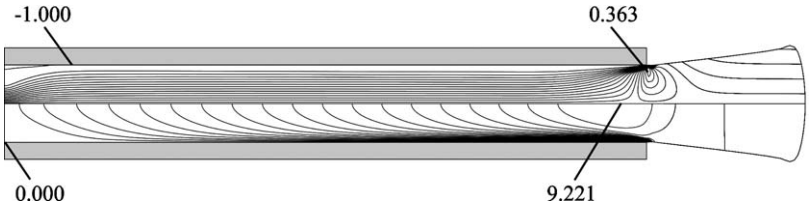

Fig. 8. Contour plots of the axial, upper half, and the radial, lower half, velocity component at $t = 0.4$ for $Bn = 100$, $Re = 0$, $Ca = 50$, $St = 0$, $w = 10$, $\varepsilon = 0.1$, $N = 300$ and under the no-slip condition.

turns the smaller and smaller stresses that it experiences as it exits the disks into larger and larger effective viscosity and thus the material becomes "frozen". As a result, it retains the thickness it had nearly when it exited and before the disks moved further towards each other. In addition, the pressure field still varies mainly in the radial direction, the main flow direction. However, its axial variation has become significant, especially near the surface of the disks, where the shear rate is strongest decreasing the effective viscosity. As time passes and the aspect ratio decreases, the pressure varies less in the axial direction following closer the lubrication theory. Again, close to the edge of the disks the pressure variation deviates from the pattern established further inside the disks. As for the shear rate, it has its smallest values near the axis of symmetry where, as we will discuss shortly, unyielded regions arise. Its largest values are close to the edge of the disks, and they decrease with time.

In order to examine the importance of the capillary forces on squeeze flow, we decreased Ca by a factor of 20 to $Ca = 50$, which is lower than the prevailing values for typical viscoplastic materials in squeeze flow, keeping the rest of the parameters as in Fig. 7. In Fig. 8, we only present the case corresponding to the intermediate time in Fig. 7, $t = 0.4$, but the behavior is the same at all times. It is very interesting that the free surface of the material is identical to that in Fig. 7b and that the maximum radial and axial velocities differ by less than 0.1% from that case. In other words, the yield stress is dominant over capillary forces, even when the latter is increased above its typical values and a rounded surface at the edge cannot be generated, in contrast to the simulations with a Newtonian fluid (Fig. 6).

Fig. 9 illustrates the time evolution of the unyielded domain for the case of a viscoplastic material with $Bn = 100$. The rest of the parameters are the same with those in Fig. 7, while the snapshots are taken at times $t = 10^{-5}$, $t = 0.2$, $t = 0.4$ and $t = 0.6$. For clarity, the solution is given between the upper disk and the midplane and only in a portion of the radial extent of the disks. The figure clearly shows that at all times the unyielded region surrounds the center of the disk surface and that there is an obvious reduction of its size with time. Smyrnaios and Tsamopoulos [16] have also noticed a decrease of the size of the unyielded domain as the aspect ratio decreases. Clearly, the different aspect ratios in their quasi-steady state analysis correspond to different time instants in our transient simulation.

Fig. 10 shows again only part of the upper quarter of the domain and the shape of the yield surface there, as a function of the Bn number under the same values for the rest of the parameters and $t = 10^{-5}$ only. As we can see, the size of the unyielded regions increases substantially with the increase of the Bn number. It is expected that viscoplasticity will have an important effect on the flow field as well. Fig. 11 shows the radial velocity profile at three different radial positions and for various Bn numbers. These profiles are taken at the first time instant of the transient simulations as well, $t = 10^{-5}$ and for the same parameter values. The profile of the radial velocity of a Newtonian fluid ($Bn = 0$) is parabolic at every radial location. However, as the Bingham number increases, the profile changes becoming flatter

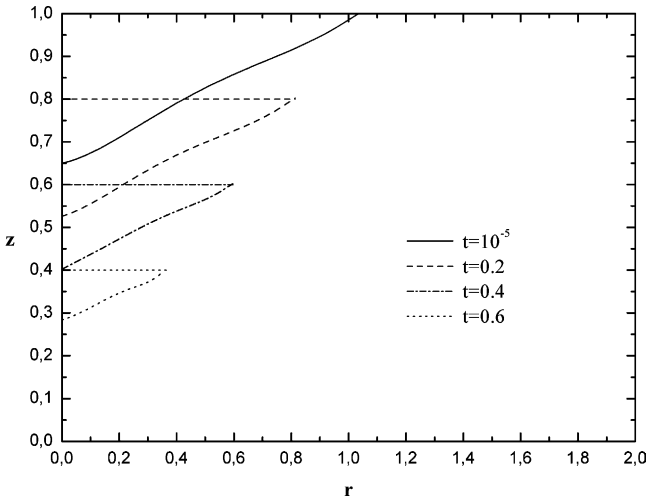

Fig. 9. Evolution of the unyielded area with time for $Bn = 100$, $Re = 0$, $Ca = 10^3$, $St = 0$, $w = 10$, $\varepsilon = 0.1$, $N = 300$ and under the no-slip condition.

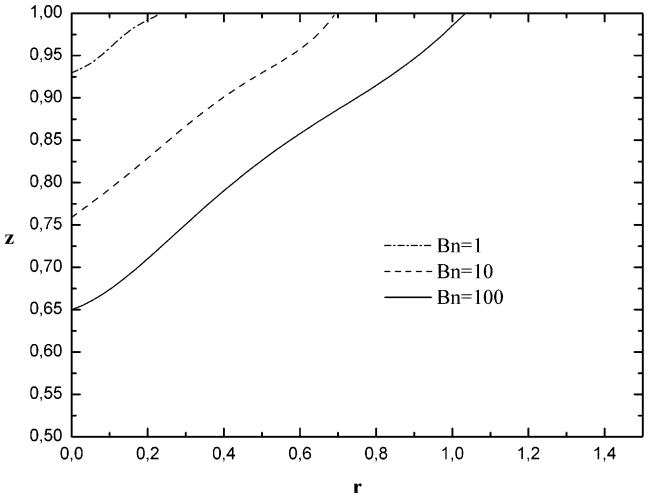

Fig. 10. Yield surfaces for $Re = 0$, $Ca = 10^3$, $St = 0$, $w = 10$, $\varepsilon = 0.1$, under the no-slip condition and various Bn numbers and the corresponding values of N as given in Table 1 at time $t = 10^{-5}$.

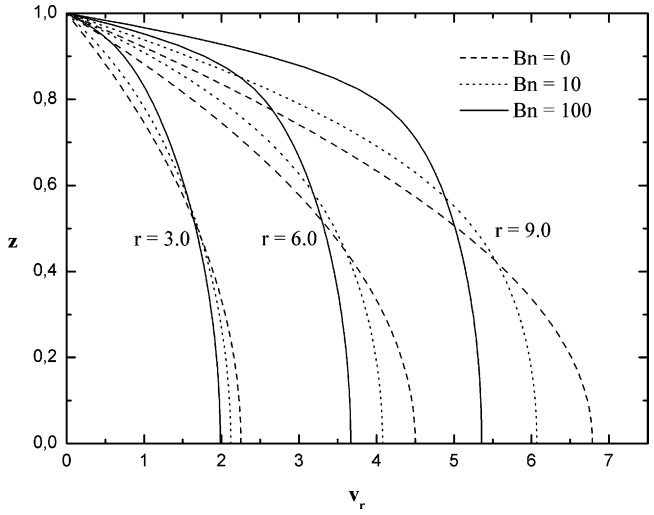

Fig. 11. Radial velocity profiles for various *Bn* numbers and the corresponding values of *N* as given in Table 1 at three different radial locations, $r = 3, 6, 9$, for $Re = 0$, $Ca = 10^3$, $St = 0$, $w = 10$, $\varepsilon = 0.1$, $N = 300$ and under the no-slip condition.

around the plane of symmetry and exhibiting a steeper increase from its zero value at the disk wall. Another demonstration of the quality of our results is given in Fig. 12. It shows either the $\dot{\gamma}$ or the pressure along the upper disk surface ($0 \le r \le 10$) and the upper free surface of the squeezed out material ($r > 10$) at two time instants. Near the center of the disks, both variables are nearly constant, while $\dot{\gamma}$ increases and P decreases monotonically with r up to the disk edge and both with a slope that increases with time. The singularity at the disk edge induces very sharp spikes in both variables, which increase with time, as expected, but are well resolved by our code. Outside the disks, both variables are nearly zero.

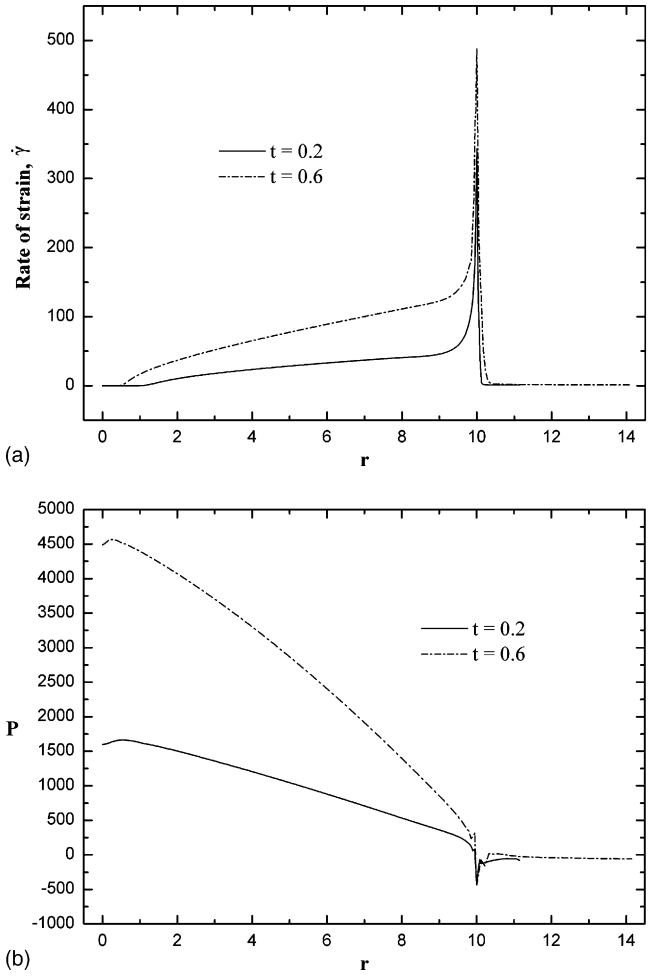

Fig. 12. Dependence of (a) the second invariant of the rate of strain $\dot{\gamma}$, (b) the pressure with the radial distance from the axis of symmetry along the disk wall and the free surface at $t = 0.2$, $t = 0.6$ for $Bn = 100$, $Re = 0$, $Ca = 10^3$, $St = 0$, $w = 10$, $\varepsilon = 0.1$, $N = 300$ and under the no-slip condition.

4.2.2. *Effect of slip*

Because of the reasons mentioned in the introduction, we studied also the effect of a slip condition at the disk wall. In particular, we chose to employ a slip model that would maximize the ratio of the slip velocity over the shear stress where the latter is largest and would smoothly reduce the slip velocity to zero away from this point. This slip model is given by Eq. (16). In a first set of simulations, we assumed that the material completely fills the volume between the disks from the beginning of the simulation. Then, the slip velocity compared to the local shear stress will be largest at the disk edge and decrease to zero towards the disk center. In a second set of simulations, we assumed that the material only partially fills the same volume and then the slip velocity will be largest at the triple contact point, but will vary in the same way in the radial direction.

Fig. 13 shows two snapshots at the same time instant, $t = 0.4$, both with $Bn = 1$, but with the no-slip condition in Fig. 13a and the slip condition in Fig. 13b. The parameter values used in the slip model are such that slip effectively takes place in a small fraction of the radius of the disks near their edge. In the first snapshot, we observe that the free surface of the material is rounded, in spite of the finite, but small value of the yield stress. In other words, its shape does not deviate too much from the Newtonian case. On the contrary, in Fig. 13b, the material outside the disk is narrower and its free surface is flatter, resembling cases with larger yield stress. The reason for this variation is that the introduction of wall-slip helps reducing the stresses in the material even before it exits the area between the disks. Thus, the effective viscosity increases locally, "freezing" the shape of the squeezed out material and surface tension is not sufficient to give it its rounded shape. This is verified by the decrease in the value of the maximum of the axial velocity by an order of magnitude and by the decrease of its variation near the exit of the disks. The magnitude and the variation of the radial velocity are not affected as much, but clearly, in Fig. 13b the radial velocity deviates from zero at the disk surface as we approach the edge of the disks.

Fig. 14 shows two snapshots under corresponding conditions, but with $Bn = 100$. Again, the introduction of the slip model makes the outer edge of the material flatter for the reasons explained above and the axial velocity never becomes positive in the upper half of the material. Its maximum value is zero at the mid-plane. Moreover, the introduction of slip reduces the stresses on the material and its high yield stress induces a more

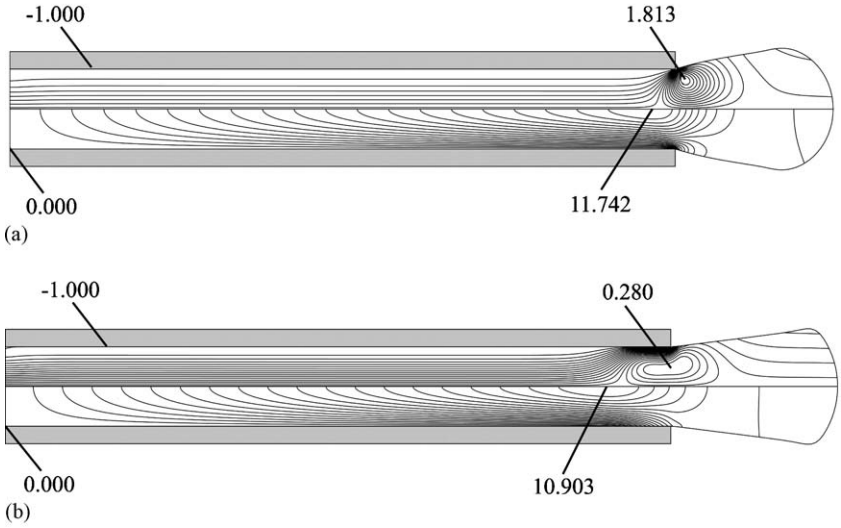

Fig. 13. Contour plots of the axial, upper half, and the radial, lower half, velocity component at time $t = 0.4$ for $Bn = 1$, $Re = 0$, $Ca = 10^3$, $St = 0$, $w = 10$, $\varepsilon = 0.1$, $N = 500$ with (a) no-slip condition, and (b) $\beta_{sl} = 1$, $\alpha_{sl} = 5$.

uniform velocity even within the disks. Their combination nullifies the mechanism leading to material swelling outside the disks to the extend that the axial velocity remains slightly negative even outside the disks but very near their edge. As in the previous case, the magnitude of the radial velocity is not affected to the same degree by the slip condition. The employment of the slip condition is confined in a region too distant from the axis of symmetry to affect the area occupied by the unyielded material. For this large value of the Bingham number this area extends axially from the disk surface to about a third of the distance to the plane of symmetry, even at this late time instant, see also Fig. 9. By closely comparing Fig. 14a with Fig. 8, we can confirm that decreasing Ca by a factor of 20 has no effect on the flow and the moving boundary.

Next, we examine the effect of placing less material than what is required to fill completely the space between the two disks. This configuration can be easily attained experimentally by first placing the material at the center of the lower disk and then lowering the upper disk until it partially squeezes the material up to the point that its radial extent is $b < a$. Fig. 15 depicts contour plots of the axial and radial velocity on the upper and lower half, respectively, at times $t = 0.2$, $t = 0.5$, $t = 0.6$ and for $Bn = 10$, $N = 500$, $w = 15$, $\varepsilon = 0.1$, and slip coefficients $\alpha_{sl} = 5$, $\beta_{sl} = 1$. Here the slip condition also helps in resolving the stress singularity at the triple contact point. At early times, the fluid moves inside the space between the disks, while later it exits this area. Soon after initiation of flow, the free surface becomes nearly parabolic with an increasing curvature as time increases and the distance between the disks decreases. One can observe that the flow field resembles the ones discussed earlier, except for an area of about 1–2 gap widths from the instantaneous position of the triple contact point. As we can see, the radial velocity

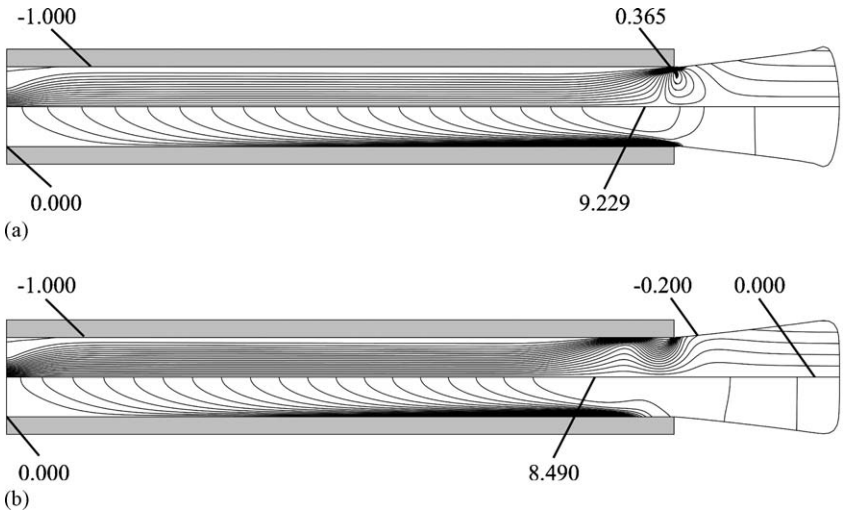

Fig. 14. Contour plots of the axial, upper half, and the radial, lower half, velocity component at time $t = 0.4$ for $Bn = 100$, $Re = 0$, $Ca = 10^3$, $St = 0$, $w = 10$, $\varepsilon = 0.1$, $N = 300$ with (a) no slip condition, and (b) $\beta_{sl} = 1$, $\alpha_{sl} = 5$.

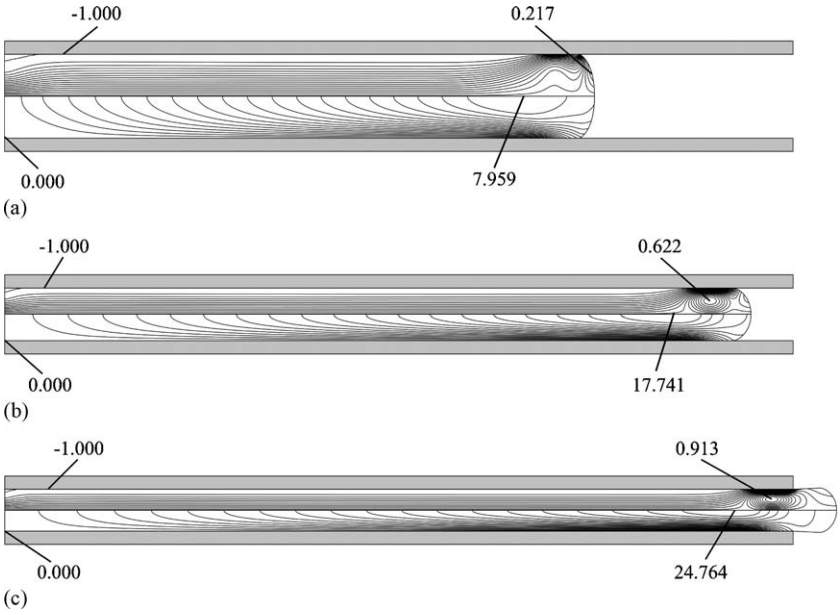

Fig. 15. Contour plots of the axial, upper half, and the radial, lower half, velocity component at $t = 0.2$, $t = 0.5$, $t = 0.6$ and for $Bn = 10$, $Re = 0$, $Ca = 10^3$, $St = 0$, $w = 15$, $\varepsilon = 0.1$, $\alpha_{sl} = 5$, $\beta_{sl} = 1$, $N = 500$.

on the surface of the disks deviates from zero in a region near the triple contact point, where slip occurs. This deviation also affects the axial velocity. Although the disks force the fluid to move in the axial direction, the fluid follows only partially their motion in the slip region because it is also allowed to slip in the radial direction. On the other hand, the axial velocity near the axis of symmetry remains equal to the velocity of the disk up to almost half the distance of the disk from the mid-plane and this happens because unyielded material arises in that region.

This can be seen more clearly in Fig. 16, where we have plotted the liquid/air interface and the yield surface for the same parameters and time instants. We can see that the viscoplastic material behaves as rigid solid around the disk center, confirming the predictions of previous researchers [14,16,23]. Moreover, one can notice that the size of the unyielded region decreases monotonically with time. This happens because as time passes and the distance between the two disks decreases, a more intense shear field is generated closer to the axis of symmetry, which forces more material to yield in that region.

It is anticipated that the flow field will depend somewhat on the values of the slip coefficients α_{sl}, β_{sl}. Fig. 17 depicts the contour plot of the axial velocity in the upper quarter of the domain between the disks for $Bn = 30$ at $t = 0.3$. In order to magnify the effect of the slip coefficients we have taken the disks to be further apart from each other, $\varepsilon = 0.5$, and the fluid between them extends only to 40% of their radius, $w = 5$, while $\alpha_{sl} = 5$ and β_{sl} is either (a) 100 or (b) 10. As mentioned earlier, the latter parameter adjusts the level of the local slip velocity in comparison to the wall shear. More specifically, when the value of β_{sl} increases the level of the slip velocity decreases. In Fig. 17a where the no-slip condition is approached the free surface is more curved and the contact angle with the disk wall is quite larger than 90°. Fig. 17b shows that as the slip velocity increases, the axial velocity becomes more uniform near the triple contact point. This makes the shape of the fluid/air interface flatter

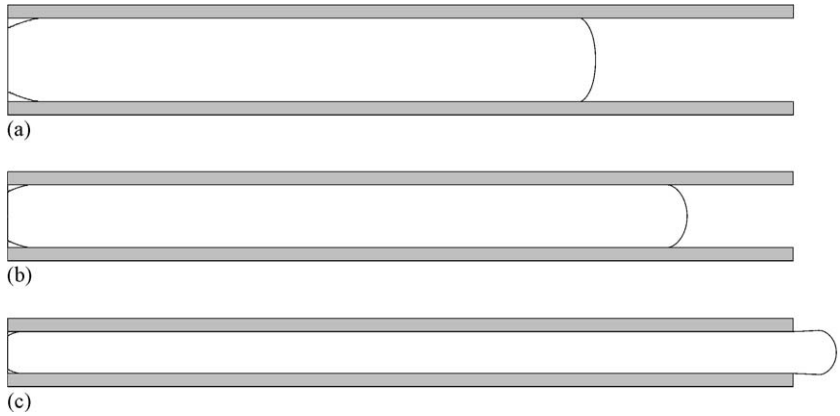

Fig. 16. Evolution of the yield surface and the material/air interface with time for $Bn = 10$, $Re = 0$, $Ca = 10^3$, $St = 0$, $w = 15$, $\varepsilon = 0.1$, $\alpha_{sl} = 5$, $\beta_{sl} = 1$, $N = 500$ at times $t = 0.2$, $t = 0.4$, $t = 0.6$.

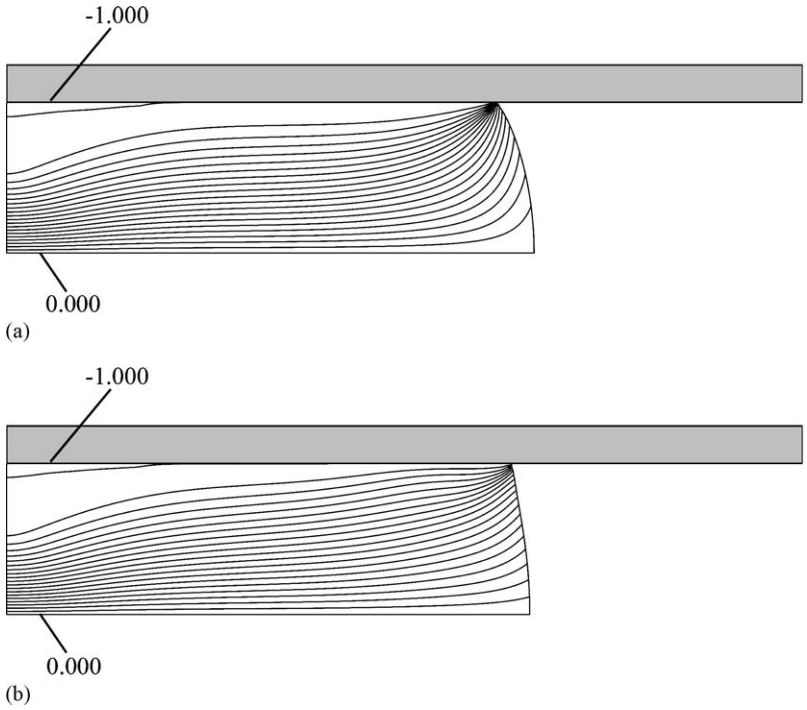

Fig. 17. Contour plots of the axial velocity at time $t = 0.3$ for $Bn = 30$, $Re = 0$, $Ca = 10^3$, $St = 0$, $w = 5$, $\varepsilon = 0.5$, $\alpha_{sl} = 5$, $N = 300$ with (a) $\beta_{sl} = 100$, and (b) $\beta_{sl} = 10$.

and the contact angle of the free surface with the disk wall approaches 90°.

We also performed simulations for different values of α_{sl}. This parameter controls the rate of decrease of the slip velocity and, consequently, it can adjust the length of the slip region. The smaller the value of α_{sl}, the larger the slip length along the wall. Simulations have shown that α_{sl}, in contrast to β_{sl}, has a small effect on the shape of the fluid/air interface, whereas it has an important effect on the size of the unyielded region. Fig. 18 shows the shape of the yield surface for two different values of α_{sl}. We observe that when the slip region is longer, the domain of the unyielded material decreases and for even smaller values, $\alpha_{sl} = 2.5$, which is not presented here, the unyielded area

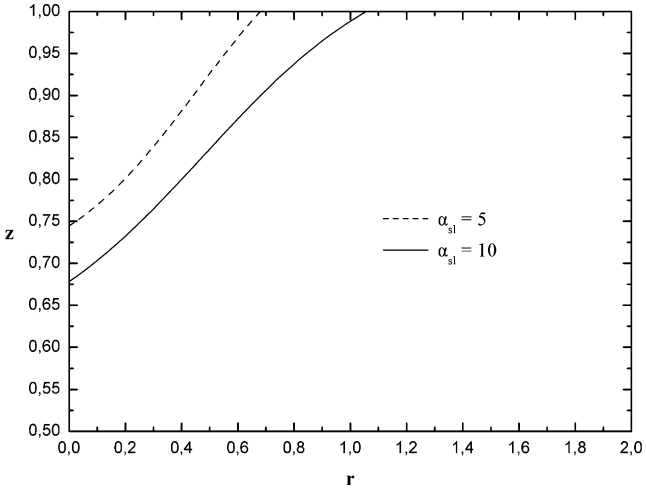

Fig. 18. Yield surfaces at time $t = 10^{-5}$ for $Bn = 30$, $Re = 0$, $Ca = 10^3$, $St = 0$, $w = 5$, $\varepsilon = 0.5$, $\beta_{sl} = 10$, $N = 300$ and different values of α_{sl}.

disappears completely. Clearly, the same would happen, if the Navier slip model was used throughout the disks, $\alpha_{sl} = 0$. This occurs because as the slip length increases and slip is allowed at a larger portion of the disk surface, the fluid follows only partially the axial motion of the disks towards the mid-plane and flows in the radial direction as well. Thus, the flow has an extensional portion even very near the disk surface and the axis of symmetry, which prohibits the formation of unyielded material.

A very general analysis of the effect of partial wall-slip on the squeeze flow problem, irrespective of the constitutive law, is presented in Ref. [36]. A most interesting result given there, based on straight-forward lubrication analysis, is that the radial velocity on the disk surface varies linearly with the radial distance assuming its maximum value at the edge of the disks, the only triple contact point in that analysis. We examined the applicability of this result in our more general case, where the triple contact point may move, the slip condition is applied in only a part of the disk surface and where the distance between the disks is rather large invalidating the lubrication assumptions. Fig. 19 shows the dependence of the radial velocity on the radial distance at various instants as obtained from our simulations. Indeed, we observe a gratifying agreement with the analysis in [36]. The radial velocity at all times remains zero where it should be, according to our slip model, but increases linearly with the radial distance where the slip condition is applied and there is a smooth transition between these two regions. Only very close to the triple point there is a slight deviation from linearity, but there the flow is not one-dimensional any more and the lubrication predictions in [36] do not apply. The radial velocity at the triple contact point increases with time simply because of mass conservation and, since the slip region remains approxi-

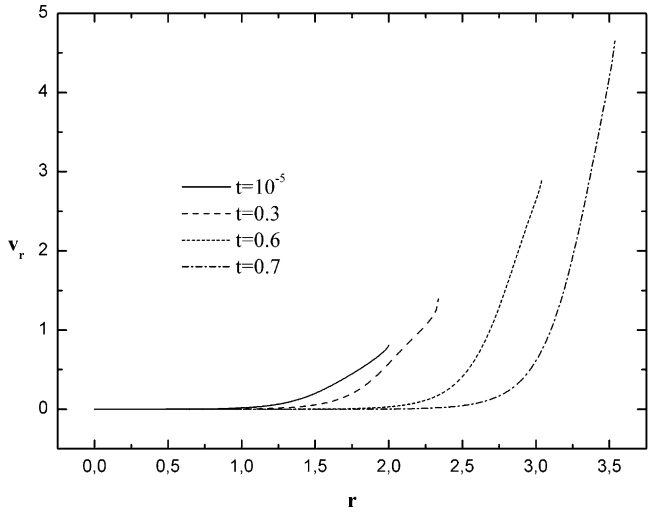

Fig. 19. Distribution of the radial velocity on the disk surface under slip conditions, $\alpha_{sl} = 5$, $\beta_{sl} = 10$ at different times, with $Bn = 30$, $\varepsilon = 0.5$, $w = 5$ and $N = 300$.

mately constant according to our slip model, the slope of the linear section increases with time as well.

4.2.3. *Effect of gravity*

Typically, the gravitational force is ignored in squeeze flow experiments on the basis that the gap is small making the Stokes number much smaller than unity. However, given the versatility of our computer code, it would be interesting to examine the effect of gravity, even if that required to place the disks further apart than what is usually the case. Even then, our simulations have shown that the flow between the disks is not affected significantly by gravity and that the most interesting effects arise when the viscoplastic material exits the area between the two disks. For this reason, we decided to present only the case where the fluid initially fills completely the space between the two disks. So we have taken $w = 2$ and $\varepsilon = 0.5$, which result in $St = 2.5$. Moreover, we assume that gravity acts downwards in the axial direction. Now, there is no plane of symmetry for the flow field and only axial symmetry can be employed to reduce the size of the examined domain. Furthermore, for convenience we assume that the lower disk is stationary and that only the upper disk moves. Of course, since $Re = 0$, this change of coordinates has no effect on the shape of the free surface or the flow field. Fig. 20 depicts the contour plots of the axial velocity at times $t = 0.5$ and $t = 0.47$ for two different values of St number and for $Bn = 5$, $\beta_{sl} = 100$, $\alpha_{sl} = 5$ and $N = 500$. As we can see in Fig. 20a and b, where $St = 0$, the flow is totally symmetric about the instantaneous mid-plane as it should be. On the other hand, one can see in Fig. 20c and d that when gravity is taken into consideration ($St = 2.5$) the flow loses its plane of symmetry and the material accelerates downwards. Although the effect of gravity is obvious outside the disks, interestingly, one could observe that the flow field between the two disks remains the same and even retains its plane of symmetry. Moreover, early on, although the flow field outside the disks is not symmetric anymore, it still resembles the one with $St = 0$ and the shape of the free surface remains almost the same. Nevertheless, later on, when more material has exited the disks, the flow field and the shape of material clearly change.

4.2.4. *Required squeeze force*

In a typical squeeze flow experiment under constant velocity, the most important measurable variable is the force that must be applied on the disks in order to maintain their velocity constant.

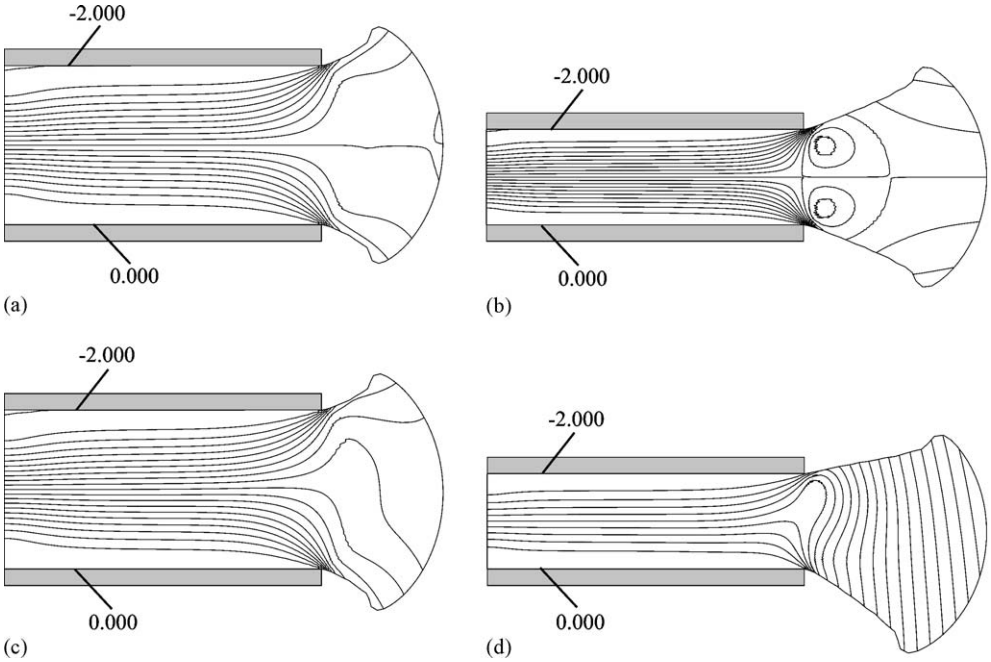

Fig. 20. Contour plots of the axial velocity at times $t = 0.5$ and $t = 0.7$ for $Bn = 5$, $Re = 0$, $Ca = 10^3$, $w = 2$, $\varepsilon = 0.5$, $\alpha_{sl} = 5$, $\beta_{sl} = 100$, $N = 500$, and $St = 0$ (for (a) and (b)) and $St = 2.5$ (for (c) and (d)).

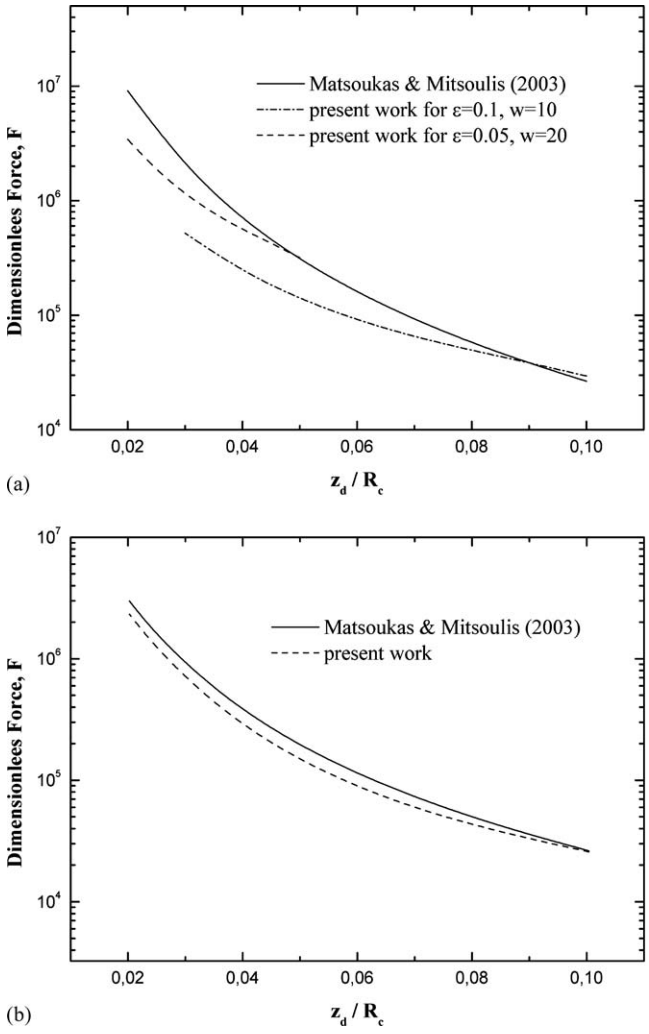

Fig. 21. Comparison of the squeeze force with the results by Matsoukas and Mitsoulis [23] for (a) $Bn = 10$, $Re = 0$, $Ca = 10^3$, $w = 10$, $\varepsilon = 0.1$, $N = 500$ and no slip condition and for (b) $Bn = 10$, $Re = 0$, $Ca = 10^3$, $w = 20$, $\varepsilon = 0.1$, $N = 500$ and the slip condition with parameter values $\alpha_{sl} = 5$, $\beta_{sl} = 1$.

We calculate this force by integrating the normal to the disks component of the total stress tensor, σ_{zz}, over the portion of the disk surface which comes into contact with the fluid, i.e. up to R_c:

$$F = \int_0^{R_c} 2\pi\sigma_{zz} r \, dr \tag{34}$$

Fig. 21a shows the comparison of our calculations for the force against the results that were given in Ref. [23] for $Bn = 10$ and $N = 500$. It must be noted that Matsoukas and Mitsoulis [23] assumed a quasi-steady state model and calculated the time independent force at different aspect ratios. Thus, in order to make the comparison possible we calculated the force at different time instants, found the corresponding ratio z_d/R_c, where z_d denotes the instantaneous axial position of the upper disk, and compared our results to theirs for the same aspect ratios. In Fig. 21a we indicate with a solid line the results from Ref. [23] and with a dash-dotted line our present results with $w = 10$, $\varepsilon = 0.1$, converted as indicated above. Clearly, the force we calculate is initially slightly higher than the one obtained from the quasi-steady state analysis, but this is easily explained by the small capillary force, acting on the perimeter of the sample, which we have included in our model, but was absent in [23]. However, as time proceeds and the disk gap decreases, the force we calculate becomes much smaller than the one resulting from a quasi-steady analysis.

The same is observed in a second simulation we performed with $w = 20$, $\varepsilon = 0.05$, i.e. by halving the disk gap, while it remains initially completely filled with material. The force is slightly larger initially, but turns much smaller later on than the corresponding one from the quasi-steady analysis. This may seem puzzling, but it can be explained by noticing that, in our dynamic simulations, the material already outside the disks has a large radial velocity and the related momentum assists the outward flow of the material still between the disks, which as a result, requires less axial force to be squeezed out. This is a very important observation and it holds irrespective of the constitutive equation for the material. It implies that, if during the squeeze flow experiment, the disk gap decreases by, say over 10%, the force measured must be adjusted accordingly, before it is compared to quasi-steady state analysis to extract rheological data. In other words, the quasi-steady state analysis cannot be applied directly and consecutively many times in order to approximate a truly unsteady experiment. In Fig. 21b, we show that we predict a smaller deviation of the applied force with our dynamic simulations from its value under the quasi-steady analysis, when the gap between them was partially filled with material and before any material exited the gap between the disks. This small deviation is probably due to the slip condition applied on the disk wall, which results in smaller velocity gradients there and especially closer to the disk exit (compare Fig. 13a and 14a to Figs. 13b and 14b).

Fig. 22a shows the dependence of the squeeze force on time and for various Bn numbers, when the gap between the disks is completely filled with material, so that $w = 10$, $\varepsilon = 0.1$. We observe that the squeeze force increases significantly with time because of the decreased distance of the disks in accordance with basic lubrication ideas. Furthermore, we notice that there is a substantial increase in the force that must be applied on the disks as the Bn number increases especially at early times. This was also noted by previous researchers [16,23]. The variation of the force is almost one order of magnitude as the Bn number increases from 1 to 100, making this experiment a valuable one for determining the yield stress for a viscoplastic fluid. Finally, Fig. 22b shows the same dependence of this force, when the slip condition is applied and when the radius of the disks is twice as that in the previous case, while the material initially occupies only part of the gap so that $w = 20$, $\varepsilon = 0.1$. Clearly, for the same Bn this force is initially smaller than that shown in Fig. 22a, because the slip condition on the disk surface facilitates the flow in every direction. However, the force now increases faster, so much so that at $t = 0.5$ it is larger than the force for the same Bn in Fig. 22a under no-slip. This occurs because in the present case, as time passes more material contacts the disk walls increasing the total resistance to flow.

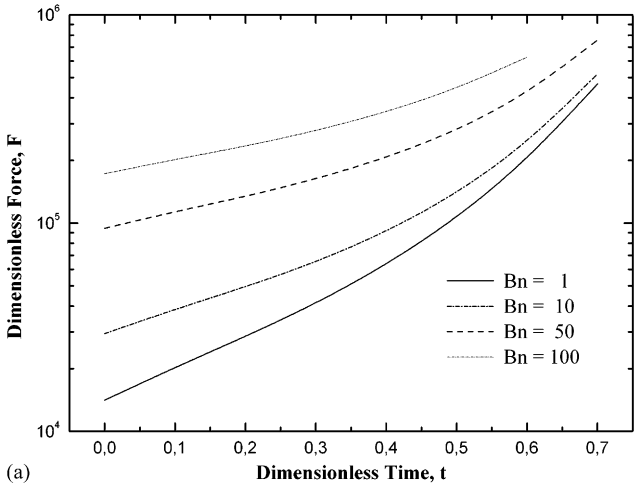

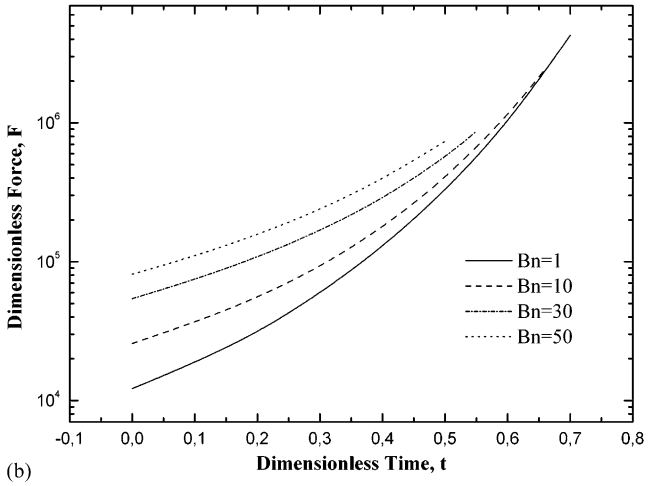

Fig. 22. Evolution of the squeeze force with time for various Bn numbers and the corresponding values of N as given in Table 1 for (a) $Re = 0$, $Ca = 10^3$, $w = 10$, $\varepsilon = 0.1$, and the no-slip condition and for (b) $Re = 0$, $Ca = 10^3$, $w = 20$, $\varepsilon = 0.1$ and the slip condition with parameter values $\alpha_{sl} = 5$, $\beta_{sl} = 1$.

4.3. Constant force case

The easiest to measure quantities in a squeeze flow experiment conducted under constant force are the axial velocity of the disks and their position as a function of time. The motion of the disks in such an experiment is decelerating because not only the resistance of the fluid continuously increases as they approach each other, according to lubrication theory, but also the effective viscosity of the material increases as the velocity and its gradients decrease. The latter effect eventually forces the disks to stop moving in a finite time. Fig. 23 shows the evolution of the axial velocity and position of the upper disk with time for the case of a viscoplastic fluid with $Bn = 50$, $w = 10$, $\varepsilon = 0.1$, and $N = 300$. Indeed, one can observe that the velocity of the disks decreases towards zero very rapidly, especially at early times. It is characteristic that the disk axial velocity has decreased by slightly over 90% from its initial value by the time $t = 0.70$, while the distance of the upper disk from the mid-plane has decreased to only $z_d \cong 0.825$. After that point the disk velocity decreases at a much smaller rate and it finally becomes practically zero

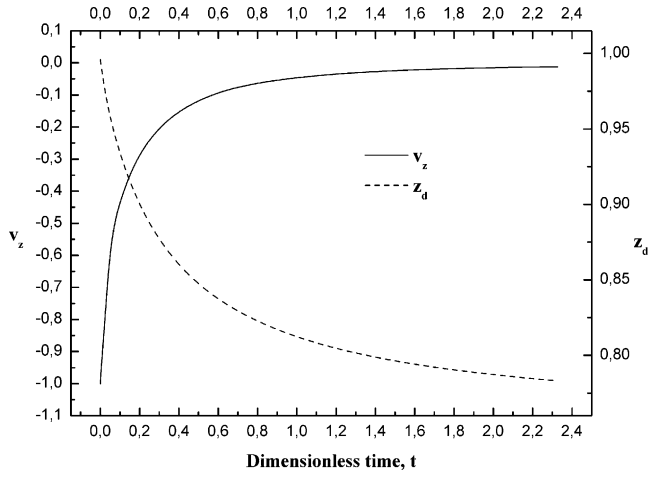

Fig. 23. Evolution of the squeeze velocity and the distance of the upper disk from the mid-plane, Z_d, with time for $Bn = 50$, $Re = 0$, $Ca = 10^3$, $w = 10$, $\varepsilon = 0.1$, $N = 300$ and under the no-slip condition.

at time $t = 2.4$. At that time instant the disk has approached a little more the plane of symmetry, $z_d \cong 0.785$. The motion of the disks essentially stops there because, as it will be shown further below, all the material beyond the edge of the two disks behaves as a rigid solid. It should be noted that having used the Papanastasiou constitutive law, which models all the material as liquid even with arbitrarily large viscosity where unyielded material should exist, the disks never stop moving, even under the constant force experiment.

Fig. 24 shows contour plots of the axial and radial velocity fields with $Bn = 10$, $w = 10$, $\varepsilon = 0.1$ at three time instants. The axial velocity varies only axially except near the axis of symmetry where the unyielded region arises and near the disk edge where the lubrication approximation fails. Both its minimum (negative) and maximum (positive) values decrease by one order of magnitude between the three snapshots. Similarly, the maximum of the radial velocity, which arises at the plane of symmetry and near the exit of the disks, decreases by an order of magnitude. This is opposite to the case of a constant velocity experiment where the maximum of the radial velocity increased with time. The curvature of the edge of the material is in between the curvature of $Bn = 1$ (Fig. 13a) and $Bn = 100$ (Fig. 14a).

Most revealing of the changing state of the material during the squeezing under constant force are the five snapshots given in Fig. 25, under the same parameter values as in Fig. 24. In the upper quarter of the domain we give the yield surface and in the lower quarter contours of $\dot{\gamma}$, as long as it takes values below 0.014 (for reasons that will become clear shortly). In these plots, we denote with a letter A and B the regions where the material behaves as solid and fluid, respectively. At the first time instant, unyielded material, according to the condition given by Eq. (32), arises only around the stagnation points of flow as in squeezing under constant velocity. This area, indicated by A_1, changes very little in the next two snapshots. The rest of the material yields and is indicated by B. As the flow decelerates everywhere, another domain with unyielded material arises at the edge of the squeezed out material and its bounding yield surface moves inwards between the second and the third snap-

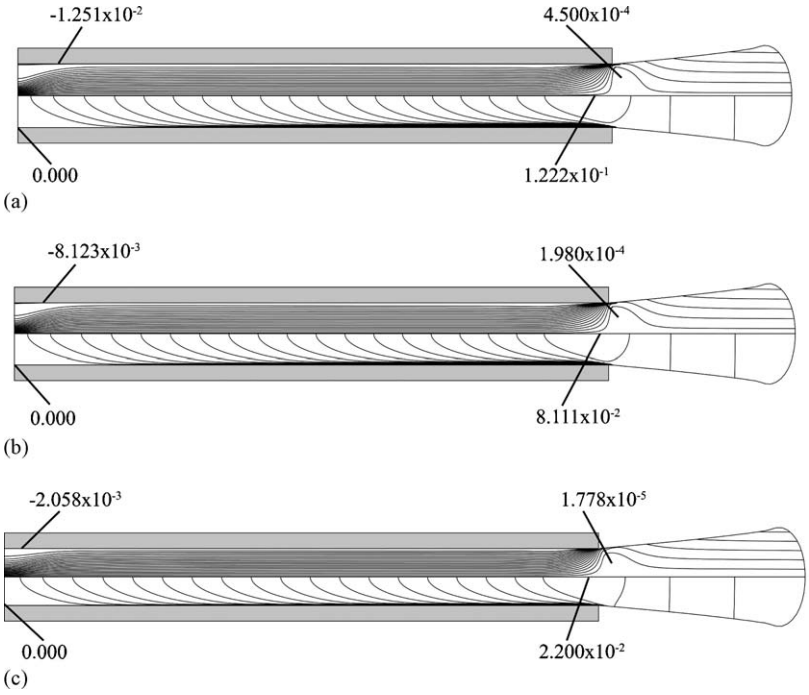

Fig. 24. Contour plots of the axial, upper half, and the radial, lower half, velocity component at $t = 5.03$, $t = 6.49$, $t = 17.16$ for $Bn = 10$, $Re = 0$, $Ca = 10^3$, $St = 0$, $w = 10$, $\varepsilon = 0.1$ and under the no-slip condition.

shot increasing this unyielded domain, which is indicated by A_2. At the fourth snapshot, the unyielded domain has moved further inwards covering a large area around the plane of symmetry, but it has not reached the axis of symmetry. Up to this instant, the domain B with yielded material is continuous and extends from the axis of symmetry all the way to slightly outside the disks, permitting flow and deformation. Finally, in the fifth snapshot the inward moving unyielded domain has merged with the unyielded domain around the disk centers. After this instant, the disks should have stopped moving and this is the point where we consider that the simulation ends. As explained earlier however, according to the Papanastasiou model, even now, finite motion of the material is allowed, albeit with very large viscosity and the condition for the yield surface given by $\tau = Bn$ is not equivalent to $\dot{\gamma} = 0$. Therefore, in principle, simulations could have continued and it should not be expected that the yield surfaces given in the upper quarter correspond to surfaces with $\dot{\gamma} = 0$ in the lower quarter. In fact, one can readily show that $\tau = Bn$ is equivalent to

$$\dot{\gamma} \exp(N\dot{\gamma}) = Bn \tag{35}$$

This dependence of $\dot{\gamma}$ on N is given in Fig. 26 for $Bn = 10$ and shows that $\dot{\gamma}$ will approach zero only asymptotically for extremely large values of N, but such values must be avoided as explained by Burgos et al. [17]. In the present case, we have taken $N = 500$ and since $\tau = Bn = 10$ at the yield surface, we find that there $\dot{\gamma} = 0.0133$, clearly $\dot{\gamma} \neq 0$. For this reason, we have plotted in Fig. 25 contours of $\dot{\gamma}$ in the lower-right quarters of the domain in the range (0, 0.014). In the first time instant, we observe that $\dot{\gamma} = 0.014$ arises just outside the unyielded material at the stagnation point, but also near the edge of the squeezed out material. In the second and third snapshots the latter domain with $0 < \dot{\gamma} \leq 0.014$ expands inwards following the displacement of the yield surface in the upper quarter. Clearly, even at the very edge of the material the even smaller value of $\dot{\gamma}$ remains $\dot{\gamma} \neq 0$ and strictly speaking very slow radial flow still occurs even there (see Fig. 24). In the fourth snapshot, values $0 < \dot{\gamma} \leq 0.014$ arise around the plane of symmetry and, in the fifth one, they reach the axis of symmetry and the two domains with $0 < \dot{\gamma} \leq 0.014$ merge. Interestingly, $\dot{\gamma}$ remains larger than 0.014 around the edge of the disks in all time instants shown. Therefore, the flow effectively stops not because all the material outside the disks becomes unyielded, but because unyielded material extends from the axis of symmetry, the stagnation points around the disk and most of the plane of symmetry all the way to its outer edge. Now we can go back and look more closely at the radial velocity profiles at three different radial positions and two time instances, the first one when unyielded material exists only around the disk centers and the second one when it covers most of the domain. These are given in Fig. 27 and clearly show that early on the velocity profile resembles that shown in Fig. 11, whereas towards the end of the experiment the radial velocity is nearly flat for the largest part of the gap between the disks. As noted already, even for $t = 17.16$ when we consider that the flow has stopped, the radial velocity is not zero at any cross section as it should, because of the employment of the Papanastasiou model.

From the practical point of view, it is important to study the effect of the Bingham number on the evolution of either the velocity or the position of the disk and, especially, their final position. For higher clarity of the results, this variation is shown in Fig. 28 by plotting the instantaneous velocity versus the instantaneous axial position of the disks, for three different values of the Bingham number and the same values for the rest

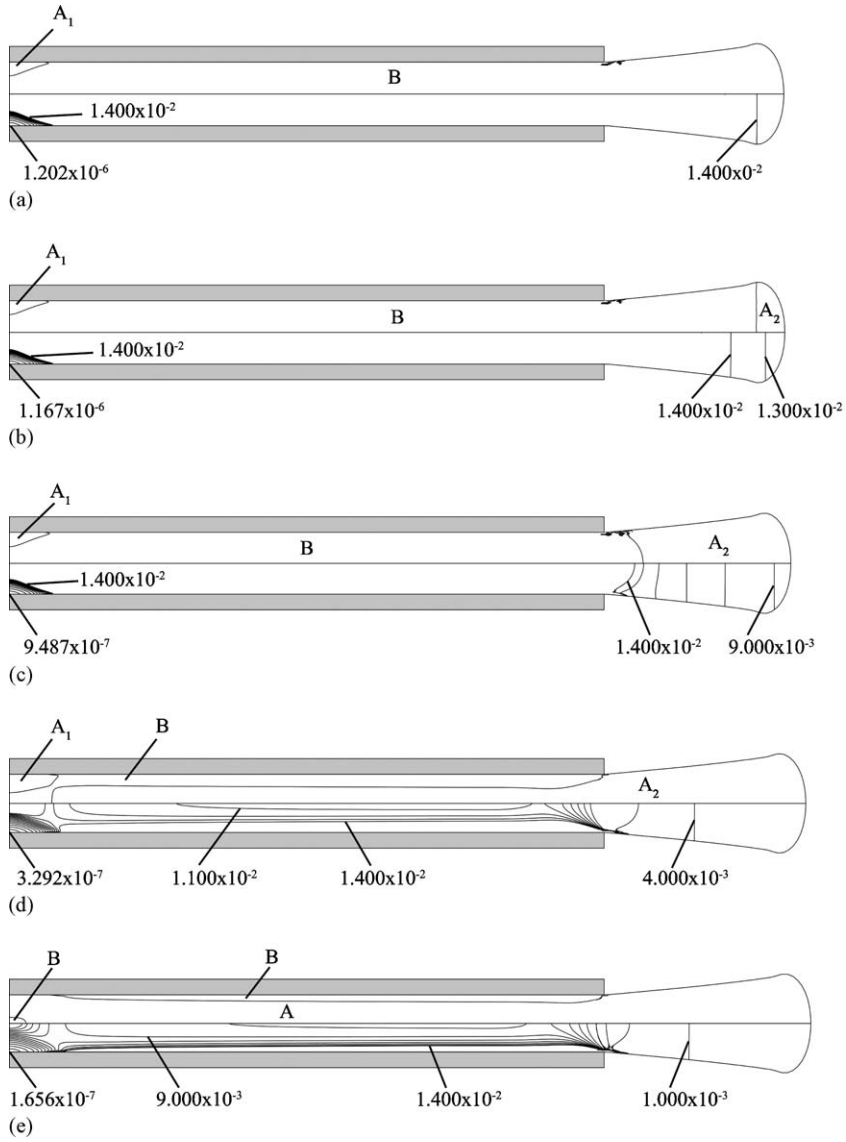

Fig. 25. Evolution of the yielded and unyielded domains, upper half, and contour plots of the second invariant of the rate of strain tensor for $0 < \dot{\gamma} \leq 0.014$, lower half, with time for $Bn = 10$, $Re = 0$, $Ca = 10^3$, $w = 10$, $\varepsilon = 0.1$, and $N = 500$, under the no-slip condition at times $t = 5.03$, $t = 5.21$, $t = 6.49$, $t = 13.06$, $t = 17.16$.

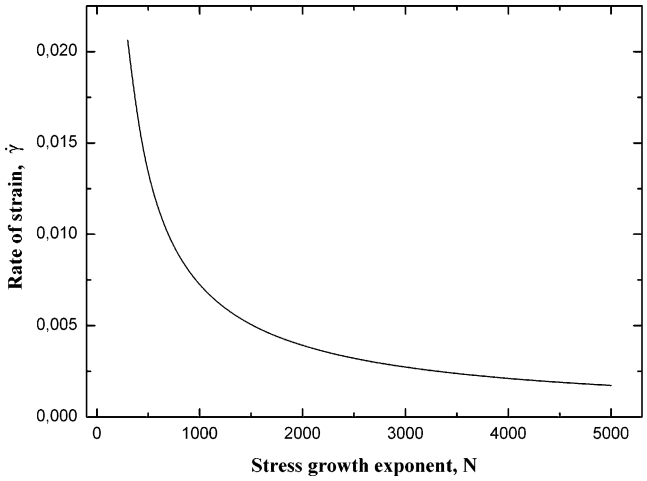

Fig. 26. Dependence of the second invariant of the rate of strain tensor at the yield surface on the stress growth exponent, N, for $Bn = 10$.

of the parameters. The calculations under constant force were performed using either 30×150 (M1) or 40×300 (M2) axial and radial elements. For the case of $Bn = 50$ it was impossible to achieve convergence with M2 and thus we performed our calculations with M1. In order to check that our solution has converged we have also performed the simulations for the case of $Bn = 10$ using both meshes M1 and M2 and as we can see in Fig. 28 the results are identical. Clearly, in the case of the lowest value of the Bingham number, $Bn = 1$, where the Newtonian behavior is approached, the disk distance can decrease to less than 15% of its initial value and their velocity seems to approach zero asymptotically. Increasing the Bingham number, forces the disks to practically stop moving before they come so close to each other and at the highest value shown here, $Bn = 50$, their motion seems to stop more abruptly. This happens because the size of the unyielded regions increases significantly with the Bn number and, consequently, these regions grow faster and merge earlier forcing the disks to finally stop moving much earlier. We

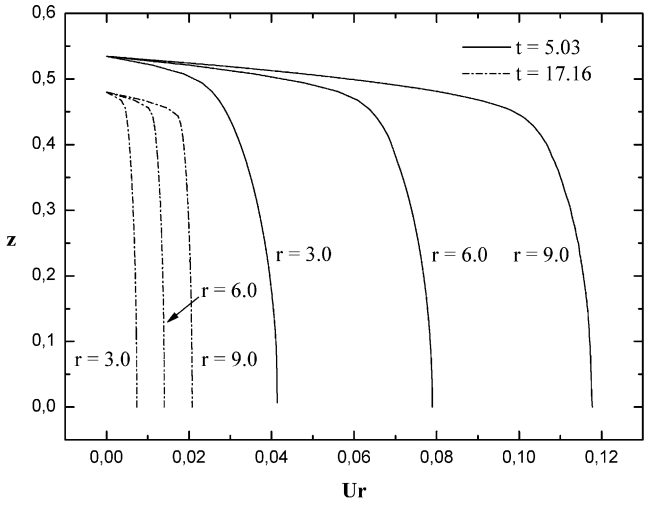

Fig. 27. Radial velocity profiles at three different radial locations $r = 3$, 6, 9 at $t = 5.03$, $t = 17.16$ for $Bn = 10$, $Re = 0$, $Ca = 10^3$, $St = 0$, $w = 10$, $\varepsilon = 0.1$, $N = 500$ and under the no-slip condition.

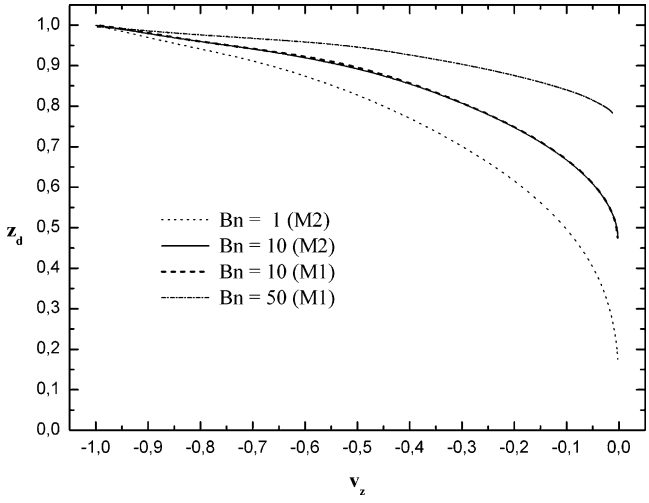

Fig. 28. Evolution of the squeeze velocity with the distance of the upper disk from the mid-plane z_d for $Re = 0$, $Ca = 10^3$, $w = 10$, $\varepsilon = 0.1$, under the no-slip condition and various Bn numbers and the corresponding values of N as given in Table 1.

believe that measuring the rate of decrease of the axial velocity of the disks and, more easily, locating the final position of the disks can become a valuable rheological test to deduce readily the yield stress of a fluid. This method for measuring the rheological properties of the material has some similarities to the one proposed in Ref. [37], and, although it is not as cheap, it provides increased control over the experimental conditions and accuracy in the measured variables. Finally, we compare the final distance as we predict it to that given in Ref. [38]. To this end, we make Eq. (2) in that reference dimensionless using our definitions for characteristic variables and find that the final half distance between the disks is

$$H_L = \frac{Bn}{3\varepsilon F} \tag{36}$$

The results are given in Table 3 and show a qualitative agreement, but the numerical values systematically overpredict the final distance and more so for the smaller Bn number. This can be attributed to the well-known deficiencies of the analysis in Ref. [38], to the possible presence of slip in the experiment and to the fact that we have employed the Papanastasiou model, which may have led us to assume cessation of disk motion somewhat prematurely. Another more recent experimental work is presented in [39]. Here the disk velocity and the disk distance are given versus time in log–log plots. We have converted our results to such plots and we obtained qualitatively the same dependence. Unfortunately, we cannot perform a quantitative comparison because the material viscosity is not reported in [39]. Moreover, we decided not to report herein extensions of our simulations to as small disk velocities as in [39], where the final velocities were 3–4 orders of magnitude smaller than the initial ones. The reason for this is that then $\dot{\gamma}$ becomes very small and the exponent, N, in the Papanastasiou model ceases to be large enough for accuracy of the simulations and fidelity of this viscoplastic model. Therefore, simulations in that low velocity range are questionable, although they exhibit even the breaking in the curve as in Fig. 7 of Ref. [39].

5. Conclusions

We examined the transient squeeze flow of a viscoplastic material between two parallel coaxial disks. Both the case of the disks moving with constant velocity and under constant force were studied. This transient simulation of squeeze flow for viscoplastic material allows us to determine the evolution of (a) the velocity and pressure fields, (b) the shape of the liquid/air interface, (c) the domain of the unyielded material and (d) the force on or the velocity of the plates. All these were impossible with the quasi-steady state models used up to now. The simulation of the process is based on the mixed finite element method for the discretization of the governing equations coupled with a quasi-elliptic mesh generation scheme in order to follow the large deformations of the physical domain.

Results from a complete parametric analysis have been presented. We examined the effect of the yield stress, the slip coefficients, the amount of material initially placed between the disks and gravity. In the constant velocity problem it is shown

Table 3
Comparison of the final distance between the disks under constant applied force as given in Ref. [38] and predicted by the present analysis (the best fit for our results is given by $H = 0.863\,[1-\exp(-0.165\,Bn^{0.687})]$)

Bingham number (Bn)	1	10	20	50	80	100
Dimensionless applied force (F)	45	94	147	301.5	452	554.7
Final distance between disks (present analysis)	0.130	0.479	0.626	0.785	0.834	0.846
Final distance between disks (Ref. [38])	0.074	0.355	0.453	0.551	0.590	0.601

that unyielded material arises around the disk centers where the two stagnation points of flow would have been, verifying previous quasi-steady state calculations. The size of these domains increases with the Bingham number, but decreases with time, because the decreased distance between the disks amplifies primarily the shear stress. The radial velocity profile changes from almost parabolic, for the case of a Newtonian fluid, to almost plug flow, as the Bingham number increases. The force that must be applied on the surface of the disks in order to maintain their constant velocity increases substantially with the Bingham number and with time. The slip condition on the surface of the disks affects the flow field only locally. Moreover, as the length of the slip region increases, the size of the unyielded area decreases significantly. Under typical gravitational conditions the flow inside the two disks is not affected appreciably, whereas when the gap between them is sufficiently large and enough fluid has exited the space between them, the effect of gravity on the flow field as well as on the shape of the free surface becomes clear.

Finally, when a constant force is applied on the disks their motion is decelerating until they finally stop, since at that time most of the material between them behaves as rigid solid. Indeed, unyielded regions arise first around the two stagnation points of flow and later on at the outer edge of the material. As time passes their size increases and they extend towards the axis and plane of symmetry, eventually merging with the former unyielded domain to form a continuous solid-like domain. The time that is needed for the disks to stop moving as well as their final position depends strongly on the viscoplasticity of the material. As the Bingham number increases, this time decreases, while the final distance between the disks increases.

Acknowledgement

This work was partially supported under the PENED program (grant number 136, starting year 2001) of the General Secretariat of Research and Technology of Greece of the Ministry of Development.

References

[1] R.B. Bird, O. Hassager, R.C. Armstrong, F.C. Curtiss, Dynamics of Polymeric Liquids: Fluid Mechanics, vol. 1, 2nd ed., John Wiley & Sons, New York, 1987.
[2] Z. Tadmor, C. Gogos, Principles of Polymer Processing, Wiley, 1979.
[3] J.D. Sherwood, G.H. Meeten, C.A. Farrow, N.J. Alderman, Squeeze-film rheometry of non-uniform mudcakes, J. Non-Newtonian Fluid Mech. 39 (1991) 311–334.
[4] M.J. Adams, B. Edmondson, D.G. Caughey, R. Yahya, An experimental and theoretical study of the squeeze-film deformation and flow of elastoplastic fluids, J. Non-Newtonian Fluid Mech. 51 (1994) 61–78.
[5] T.W. Chan, D.G. Baird, An evaluation of a squeeze flow rheometer for the rheological characterization of a filled polymer with a yield stress, Rheol. Acta 41 (2002) 245–256.
[6] G.H. Meeten, Yield stress of structured fluids measured by squeeze flow, Rheol. Acta 39 (2000) 399–408.
[7] G.H. Meeten, Constant-force squeeze flow of soft solids, Rheol. Acta 41 (2002) 557–566.
[8] C. Servais, A. Luciani, J.A.E. Manson, Squeeze flow of concentrated long fibre suspensions experiments and model, J. Non-Newtonian Fluid Mech. 104 (2002) 165–184.
[9] R.B. Bird, G.C. Dai, B.J. Yarusso, The rheology and flow of viscoplastic materials, Rev. Chem. Eng. 1 (1983) 1–70.
[10] H.A. Barnes, The yield stress – a review or 'παντα ρει' – everything flows? J. Non-Newtonian Fluid Mech. 81 (1999) 133–178.
[11] E.C. Bingham, Fluidity and Plasticity, McGraw-Hill, 1922.
[12] A.N. Beris, J.A. Tsamopoulos, R.C. Armstrong, R.A. Brown, Creeping motion of a sphere through a Bingham plastic, J. Fluid Mech. 158 (1985) 219–244.
[13] M.A. Moyers-Gonzalez, I.A. Frigaard, Numerical solution of duct flows of multiple visco-plastic fluids, J. Non-Newtonian Fluid Mech. 122 (2004) 227–241.
[14] E.J. O'Donovan, R.I. Tanner, Numerical study of the Bingham squeeze film problem, J. Non-Newtonian Fluid Mech. 15 (1984) 75–83.
[15] T.C. Papanastasiou, Flows of materials with yield, J. Rheol. 31 (1987) 385–404.
[16] D.N. Smyrnaios, J.A. Tsamopoulos, Squeeze flow of Bingham plastics, J. Non-Newtonian Fluid Mech. 100 (2001) 165–190.
[17] G.R. Burgos, A.N. Alexandrou, N.M. Entov, On the determination of yield surfaces in Herschel–Bulkley fluids, J. Rheol. 43 (3) (1999) 463–483.
[18] H.A. Barnes, K. Walters, The yield stress myth? Rheol. Acta 24 (1985) 323–326.
[19] P. Jay, A. Magnin, J.M. Piau, Viscoplastic fluid flow through a sudden axisymmetric expansion, AIChE J. 47 (10) (2001) 2155–2166.
[20] J.A. Tsamopoulos, M.F. Chen, A.V. Borkar, On the spin coating of viscoplastic fluids, Rheol. Acta 35 (1996) 597–615.
[21] Y. Dimakopoulos, J. Tsamopoulos, Transient displacement of a viscoplastic material by air in straight and suddenly constricted tubes, J. Non-Newtonian Fluid Mech. 112 (2003) 43–75.
[22] G.G. Lipscomb, M.M. Denn, Flow of Bingham fluids in complex geometries, J. Non-Newtonian Fluid Mech. 14 (1984) 337–346.
[23] A. Matsoukas, E. Mitsoulis, Geometry effects in squeeze flow of Bingham plastics, J. Non-Newtonian Fluid Mech. 109 (2003) 231–240.
[24] H. Mavridis, G. Bruce, G. Vansco, G. Weatherly, J. Vlachopoulos, Deformation patterns in the compression of polypropylene disks: experiments and simulation, J. Rheol. 36 (1992) 27–43.
[25] H.A. Barnes, A review of the slip (wall depletion) of polymer solutions, emulsions and particle suspensions in viscometers: its cause, character, and cure, J. Non-Newtonian Fluid Mech. 56 (1995) 221–251.
[26] G.C. Georgiou, M.J. Crochet, Time-dependent compressible extrudate-swell problem with slip at the wall, J. Rheol. 38 (1994) 1745–1755.
[27] J.M. Piau, N. El Kissi, Measurement and modeling of friction in polymer melts during macroscopic slip at the wall, J. Non-Newtonian Fluid Mech. 54 (1994) 121–142.
[28] M.R. Kamal, S.K. Goyal, E. Chu, Simulation of injection mold filling of viscoelastic polymer with fountain flow, AIChE J. 34 (1) (1988) 94–105.
[29] C.L.M.H. Navier, Memoire sur le lois du mouvement des fluids, Acad. R. Sci. Inst. Fr. 6 (1823) 389–440.
[30] Y. Dimakopoulos, J. Tsamopoulos, A quasi-elliptic transformation for moving boundary problems with large anisotropic deformations, J. Comp. Phys. 192 (2003) 494–522.
[31] Y. Dimakopoulos, J. Tsamopoulos, Transient displacement of a Newtonian fluid by air in straight or suddenly constricted tubes, Phys. Fluids 15 (7) (2003) 1973–1991.
[32] Y. Dimakopoulos, J. Tsamopoulos, On the gas-penetration in straight tubes completely filled with a viscoelastic fluid, J. Non-Newtonian Fluid Mech. 117 (2004) 117–139.
[33] K.J. Ruschak, A method for incorporating free boundaries with surface tension in finite element fluid-flow simulators, Int. J. Numer. Meth. Eng. 15 (1980) 639–648.
[34] A.J. Poslinski, J.A. Tsamopoulos, Inflation dynamics of fluid annular menisci inside a mold cavity. I. Deformation driven by small gas pressure, Chem. Eng. Sci. 46 (1) (1991) 215–232.

[35] A. Poslinski, J. Tsamopoulos, Nonisothermal parison inflation in Blow molding, AIChE J. 36 (12) (1990) 1837–1850.
[36] H.M. Laun, M. Rady, O. Hassager, Analytical solutions for squeeze flow with partial wall slip, J. Non-Newtonian Fluid Mech. 81 (1999) 1–15.
[37] N. Pashias, D. Boger, J. Summers, D. Glenister, A fifty cent rheometer for yield stress measurement, J. Rheol. 40 (6) (1996) 1179–1189.
[38] G. Covey, B. Stanmore, Use of the parallel plate plastometer for the characterization of viscous fluids with yield stress, J. Non-Newtonian Fluid Mech. 8 (1981) 249–260.
[39] G.H. Meeten, Effects of plate roughness in squeeze-flow rheometry, J. Non-Newtonian Fluid Mech. 124 (2004) 51–60.